**Title**
Ageostrophic Instabilities of Interior Horizontal and Vertical Shear Flows

**Author**
Wang, Peng

**Publication Date**
2012

UNIVERSITY OF CALIFORNIA
Los Angeles

# Ageostrophic Instabilities of Interior Horizontal and Vertical Shear Flows

A dissertation submitted in partial satisfaction
of the requirements for the degree
Doctor of Philosophy in Atmospheric and Oceanic Sciences

by

**Peng Wang**

2012

## ABSTRACT OF THE DISSERTATION

# Ageostrophic Instabilities of Interior Horizontal and Vertical Shear Flows

by

**Peng Wang**

Doctor of Philosophy in Atmospheric and Oceanic Sciences
University of California, Los Angeles, 2012
Professor James. C. McWilliams, Chair

This dissertation mainly addresses the generic types of ageostrophic instability in general continuously differentiable, interior, horizontal and vertical shear flows without special ”edges” (vertical, side or equatorial boundaries or frontal outcropping). In contrast to the classic barotropic and baroclinic instabilities, whose nonlinear dynamics (geostrophic turbulence) have an “inverse cascade” characteristic, the ageostrophic instabilities serve as a local route for the breakdown of balance in the interior ocean or atmosphere, leading to an efficient energy cascade towards small scales. For the first part of this dissertation, the linear instabilities, both momentum-balanced and unbalanced, in several different $\overline{u}(y)$ shear profiles are investigated in the rotating shallow water equations. The unbalanced instabilities are strongly ageostrophic and involve inertia-gravity wave motions, occurring only for finite Rossby ($Ro$) and Froude ($Fr$) numbers. Aside from the classic shear instability among balanced shear wave modes (i.e., B-B type), two types of ageostrophic instability (B-G and G-G) are found. Here B represents balanced shear wave mode, and G represents inertia-gravity wave mode. The B-G instability has attributes of both a balanced shear wave mode and an inertia-gravity wave mode. The G-G instability occurs as a sharp resonance between two inertia-gravity wave modes. The criterion for the occurrence of the ageostrophic instability is associated with the second stability condition of *Ripa* [1983], which requires a sufficiently large local Froude number. When $Ro$ and especially $Fr$ increase, the balanced instability is suppressed, while the ageostrophic instabilities are enhanced. The profile of the mean flow also affects the strength of the balanced and ageostrophic instabilities. For the second part of this dissertation, the linear instabilities of several rotating, stably stratified, interior vertical shear flows $\overline{U}(z)$ are solved in Boussinesq equations. Two types of baroclinic, ageostrophic instability, AI1 and AI2, are found in antisymmetric $\overline{U}(z)$ for intermediate Rossby number ($Ro$). AI1 is a stationary (zero frequency) instability, which appears in a continuous transformation of the unstable mode properties between classic baroclinic instability (BCI) and centrifugal instability (CI). It begins to occur at intermediate $Ro$ values and horizontal wave numbers ($k$, $l$) that are far from $l = 0$ or $k = 0$. AI1 grows by drawing energy from the kinetic energy of the mean flow. The instability AI2 always has inertial critical layers at certain heights; and hence it is associated with an inertia-gravity wave. For an unstable AI2 mode, the coupling is either between an interior balanced shear wave and an inertia-gravity wave (B-G), or between two inertia-gravity waves (G-G). The main energy source for an unstable B-G mode is the mean kinetic energy, while the main energy source for an unstable G-G mode is the mean available potential energy. AI1 and AI2 of the B-G type occur in the neighborhood of $A - S = 0$ [*McWilliams et al.*, 1998], while AI2 of the G-G type arises beyond this condition ($A - S$ denotes absolute vertical vorticity minus strain rate in isentropic coordinates). Both AI1 and AI2 are unbalanced instabilities, which lead to a loss of balance in 3D interior flows.

The dissertation of Peng Wang is approved.

Jonathan Aurnou

Alex Hall

C. Roberto Mechoso

James. C. McWilliams, Committee Chair

University of California, Los Angeles
2012

*To my parents and husband . . .*

*for their endless love and support*

# Table of Contents

# LIST OF FIGURES

# LIST OF TABLES

# ACKNOWLEDGMENTS

My deepest gratitude goes to my dissertation advisor, Prof. James C. McWilliams, for his guidance, support and encouragement in my research life. He is always there when I need help on my research project. He has been teaching me how to strengthen myself in both ability and personality to be an independent researcher. I have benefited a lot from his physical ideas and profound knowledge, and also learned to be brave, patient and active when confronted with problems and failure in my work.

I really appreciate fellow colleagues, Junhong Liang, Claire Ménesguen, Jeroen Molemaker and Alexander Shchepetkin, who share their precious experiences and give me helpful suggestions. I greatly appreciate Diana McWilliams for spending a lot of time on editing and improving my writings, Prof. Ziv Kizner for the helpful comments on my research paper, and Prof. Jonathan Mitchell for many helpful scientific discussions. I would like to thank my committee members Prof. Roberto Mechoso, Prof. Alex Hall, and Prof. Jonathan Aurnou for helpful comments on my dissertation.

I would like to express my sincere thanks to my husband, Lunjin Chen, and my parents for endless love and support through all my good and hard times. I would also like to thank my good friends, Yujie Tang and Hwajin Kim, who share my happiness and difficulty in the past five years.

My work was partially supported by the National Science Foundation (OCE-1049134) and Office of Naval Research (N00014-10-1-0484).

# VITA

| | |
|---|---|
| 2003–2007 | B.S. in Physics, Peking University, China. |
| 2007–2008 | M.S. in Atmospheric and Oceanic Sciences, UCLA, USA. |
| Spring 2009 | Teaching Assistant, Department of Atmospheric and Oceanic Sciences, UCLA, USA. |
| 2008-2012 | Ph.D., Department of Atmospheric and Oceanic Sciences, UCLA, USA. |

# PUBLICATIONS

**Wang, P.**, McWilliams, J. C., and Ménesguen, C. 2012 Ageostrophic instability in rotating, stratified interior vertical shear flows. *J. Fluid. Mech.* In preparation.

**Wang, P.**, McWilliams, J. C., and Kizner, Z. 2012 Ageostrophic instability in rotating shallow water. *J. Fluid. Mech.* In Press.

Liang, J., McWilliams, J. C., Kurian, J., Colas, F., **Wang, P.**, and Uchiyama, Y. 2012 Mesoscale variability in the northeastern tropical Pacific: Forcing mechanisms and eddy properties. *J. Geophys. Res.*, 117, C07003.

Nie, J., **Wang, P.**, Yang, W., and Tan, B. 2008 Northern hemisphere storm tracks in strong AO anomaly winters. *Atmos. Sci. Lett.*, 9, 153-159.

# CHAPTER 1

# Introduction

## 1.1 Balanced Dynamics and Loss of Balance

The general circulation of the ocean is constrained by approximately "balanced" dynamics, i. e., mostly geostrophic in horizontal momentum and hydrostatic in vertical momentum. The circulation is strongly influenced by rotation ($f \neq 0$) and stable stratification ($N^2 > 0$), with a small Rossby number $Ro = U_0/fL$ and Froude number $Fr = U_0/NH$, where $U_0$ is the characteristic velocity scale, $f$ and $N$ are Coriolis and buoyancy frequencies, and $L$ ($H$) is the horizontal (vertical) length scale. For mesoscale eddies in the ocean, the $Ro$ and $Fr$ are typically not large, and they are also approximately balanced motions. The balanced dynamics belong to the "slow manifold" of advection and potential vorticity dynamics, which are manifested by an approximate model called Balanced Equations. As $Ro \rightarrow 0$, quasi-geostrophic equations are asymptotically accurate as Balanced Equations. For finite $Ro$, the Balanced Equations manifest a higher-order momentum balance (e.g., gradient-wind balance) [*Charney*, 1962, *Lorenz*, 1960]. In contrast, the "fast manifold", which is excluded from the balanced dynamics, is categorized as "unbalanced" motions, whose primary paradigm is inertia-gravity waves. The general circulation is forced on the planetary scale, and the majority of kinetic and available potential energy is maintained on the planetary and mesoscale scales. On the other side, the kinetic energy dissipation is only effective on the molecular scale. How is the energy transferred towards small scales and finally dissipated? The nonlinear dynamics in the balanced flows, geostrophic turbulence, is understood to be a very inefficient route due to its "inverse cascade" [*Charney*, 1971]. Therefore, breakdown of balance, manifested as an energy transfer to unbalanced motions, can be an important route for a forward turbulent energy cascade and dissipation.

The boundary regions (e.g., turbulent boundary layer, bottom topography, and coast) are generally known as places where the flows lose their balance and dissipation occurs. However, the dissipation of energy in boundary regions is not enough to cover the whole water volume in the ocean. Figure 1.1 presents the major energy reservoirs, their sources and interchanges in the ocean based on the estimation from observation. Green denotes primarily ageostrophic motions, blue denotes the motions that are dominantly in geostrophic balance, and red denotes forcing. Besides the solar and lunar tidal cycle (the left energy route in the figure), most of the energy which drives the general circulation comes from the surface wind and heat forcing. Note that most of the wind flux work (68TW out of 69TW) is dissipated right away by the surface wave breaking, and hence this fraction of wind forcing is not involved in maintaining the circulation. A majority of the forcing energy that participates in the general circulation (0.8TW out of 1TW) finally goes to the interior ocean that is roughly below 100m (below the boundary mixed layer). The interior ocean is a big reservoir of kinetic and available potential energy, but the mechanisms and rates for the energy dissipation there through the loss of balance is still unclear (indicated by the yellow box along the right energy route). The eddy diffusivity (or dissipation rate) is a necessary and important parameter in the large-scale ocean models. Many schemes that proposed for the parameterization of eddy diffusivity are for turbulent boundary layers. The interior eddy diffusivity is much less studied hence poorly determined [*Bryan*, 1987, *Gargett*, 1984], mainly due to the difficulty to reach high-resolution observation in the interior ocean, and the incomplete understanding of the small-scale dynamics there. Studying the mechanism how the energy is transferred from the balanced mesoscale eddies to those unbalanced fluctuations in the interior ocean can help us to have a clearer knowledge of submesoscale dynamics and further do a better job on the eddy diffusivity parameterization.

Therefore, identifying a local route for a loss of balance and forward energy cas-

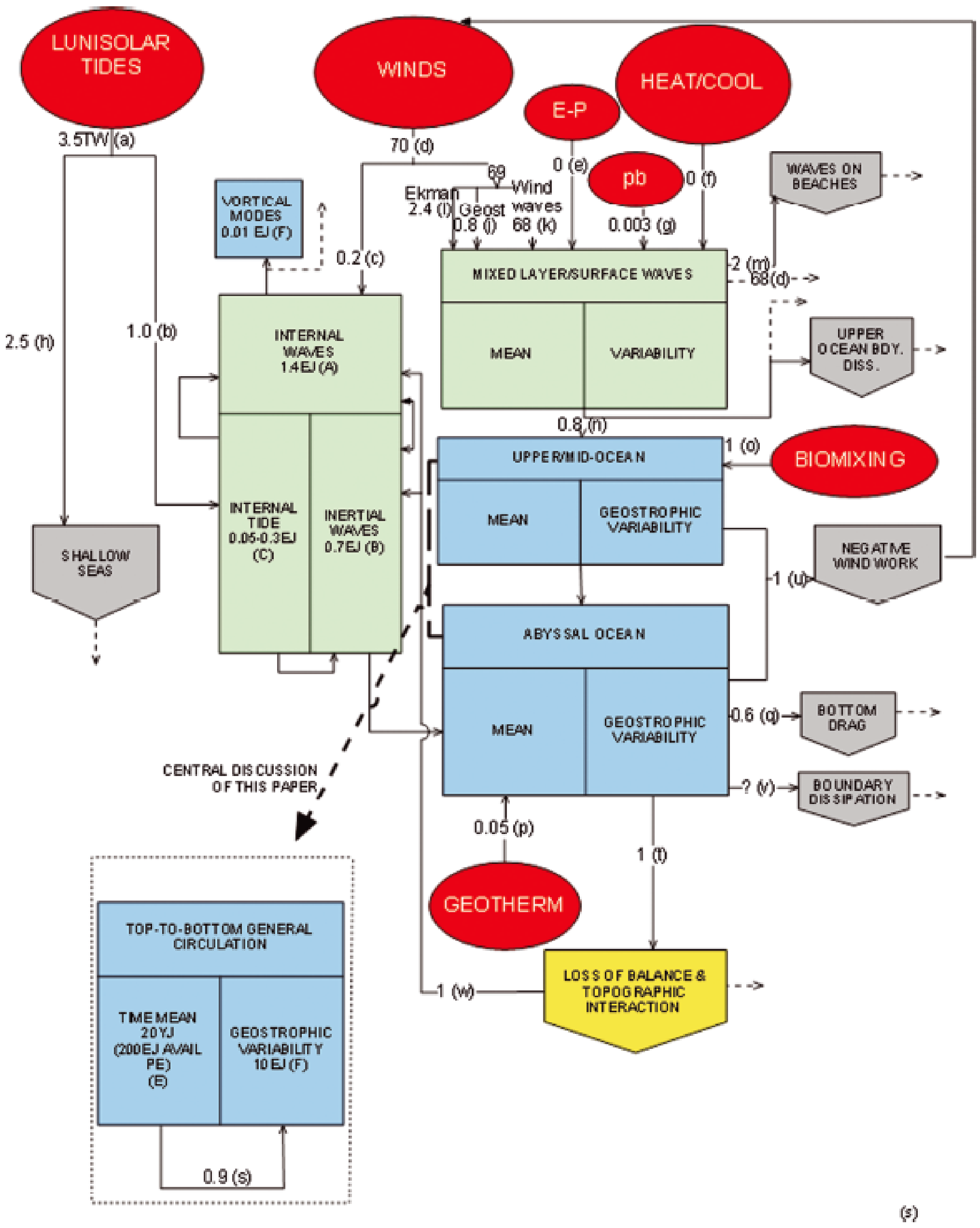

Figure 1.1: A presentation of the major energy reservoirs, their sources and interchanges for the ocean. Transfers are in terawatts (TW = $10^{12}$W), and reservoir values are in exajoules (EJ = $10^{18}$J) except for the time-mean general circulation which is in yottajoules (YJ = $10^{24}$J). More explanation about the figure is in the text part of Sec. 1.1. Figure from *Ferrari and Wunsch* [2010].

cade in the interior ocean is an important, fundamental geophysical fluid dynamical problem. It is not yet generally understood. The classic barotropic [*Drazin and Reid*, 1981, *Poulin and Flierl*, 2003] and baroclinic [*Charney*, 1947, *Eady*, 1949, *Phillips*, 1954] instabilities, which are associated with the inflection point (where potential vorticity gradient changes sign) in the velocity profile [*Rayleigh*, 1880], occur within the constraints of balance, hence are not likely to be a route for the breakdown of balance. The purpose of our work is to look for possible types of ageostrophic instability that can provide a local route to a loss of balance in the interior flows.

## 1.2 Ageostrophic Instabilities

There are a few types of classic ageostrophic instability that have been well studied. Gravitational instability [*Chandrasekhar*, 1961], which occurs when the stratification is unstable ($N^2 < 0$), is a very early stage for the convective turbulence. Centrifugal instability [*Ooyama*, 1966] occurs where the Ertel potential vorticity changes sign ($PV_{Ertel} < 0$); it greatly enhances the local vertical motions. Kelvin-Helmholtz instability [*Miles*, 1961] starts when there is strong vertical shear in a stratified flow ($Ri = N^2/U_z^2 < \frac{1}{4}$, where $Ri$ is Richardson number), and it induces vertical overturning and diapycnal mixing. These ageostrophic instabilities were originally identified in a non-rotating regime and have been well examined in laboratory experiments. Other than these classic ones, the previous literature has proposed a couple of theoretical frameworks and identified several types of ageostrophic instability.

### 1.2.1 Theoretical Framework

*Ripa* [1983] derives two sufficient stability conditions for a rotating shallow water parallel flow: if there exists any constant value of $\alpha$ such that $[\alpha - U(y)]dQ(y)/dy \geqslant 0$ and $[\alpha - U(y)]^2 \leqslant H(y)$ for all $y$, then the flow is stable to infinitesimal perturbations. Here $U(y)$, $H(y)$ and $Q(y)$ are the mean flow velocity, total water depth and potential vorticity, respectively. His first condition is related to the Rayleigh's inflection point criterion (associated with the barotropic instability), and the second one refers to a local Froude number $Fr$ condition. The second condition by *Ripa* [1983] provides us a theoretical direction on the ageostrophic instability in rotating shallow water or hydrostatic layered flows. The conditions are generalized by *Ripa* [1991] in a multi-layer model; however, they cannot be asymptotically applied to a continuously stratified fluid due to its lack of a lower bound on the inertia-gravity wave horizontal phase speed at high wavenumber, in contrast to a shallow-water fluid with lower bounds on both its vertical length scale and horizontal phase speed.

*McWilliams et al.* [1998] proposed three sufficient conditions for the occurrence of the breakdown of balanced evolution in a 3D stratified flow, which are associated with three types of ageostrophic instability. These conditions are: 1) sign change of stratification $N^2$, which is related to the gravitational instability; 2) sign change of the absolute vertical vorticity on isentropic surfaces $A$ (proportional to $PV_{Ertel}$), which is related to the centrifugal instability; 3) sign change of $A-S$, where $S$ is the magnitude of horizontal strain rate in the isentropic coordinates, hence it is necessarily positive. The third condition can be satisfied in more common situations, with a moderate but finite $Ro$. Because $A$ tends to be small in anticyclonic flows, the instabilities that are relevant to the $A - S$ condition are often called anticyclonic, ageostrophic instability (AAI). Unlike the other two criteria ($N^2 = 0$ and $A = 0$), the occurrence of AAI may be in the neighborhood of, rather than precisely at, $A-S = 0$. The above three conditions require a fully 3D structure of the unstable modes, hence are more relevant to the ageostrophic instabilities in a 3D stratified flow than the *Ripa* [1983] condition for a shallow water layer.

### 1.2.2 Earlier Studies on Ageostrophic Instability

Several types of ageostrophic instability have been identified in shallow water or hydrostatic layered flows. In a non-rotating shallow water model, *Satomura* [1980] and *Balm-*

*forth* [1999] study wall-bounded flows (a Couette flow with zero potential-vorticity gradient and a hyperbolic tangent flow with small potential-vorticity gradient, respectively), suggesting there is an instability when the gravity waves resonate. With a radiating boundary condition, *Satomura* [1980] also identifies a type of radiating unable gravity waves. In an equatorial, zero potential vorticity front, *Hayashi and Young* [1987] find a type of ageostrophic instability triggered by the resonance between two Kelvin waves. *Dritschel and Vanneste* [2006] examine a geostrophic potential vorticity front and find a weakly unstable ageostrophic mode that is associated with the potential vorticity discontinuity and far-field inertia-gravity waves. Beginning with *Orlanski* [1968] and *Mechoso and Sinton* [1983], who study a variety of instabilities in a long-wave limit with a two-layer frontal model, both geostrophic and ageostrophic instabilities are found in a geostrophic surface-frontal flow, a. k. a., a flow with a vanishing layer depth where the bounding interface "outcrops" (and quasigeostrophic theory based on $Ro, Fr \to 0$ fails). The frontal-trapped mode is stable in a one-layer shallow water frontal flow with uniform potential vorticity [*Paldor*, 1983]. With another nearby front or non-uniform potential vorticity in the flow, the frontal mode becomes unstable, by interacting with another frontal mode or the shear mode [*Griffiths et al.*, 1982, *Kubokawa*, 1985]. With a nearby side boundary, the interaction of the frontal-trapped mode and the coastal-trapped mode (Kelvin wave mode) leads to an ageostrophic instability [*Gula and Zeitlin*, 2010, *Kubokawa*, 1986]. With the addition of an active second layer, the frontal flow has non-uniform potential vorticity, and the frontal mode, the shear mode, and the gravity wave mode lead to different combinations of resonance with several types of instability [*Boss et al.*, 1996, *Gula et al.*, 2010, *Killworth et al.*, 1984]. *Sakai* [1989], followed by *Gula et al.* [2009a,b], and *Sutyrin* [2007], finds a type of ageostrophic instability caused by a resonance between a shear wave and a boundary Kelvin wave in a channeled, purely baroclinic, two-layer hydrostatic flow. *Iga* [1999] extends the *Sakai* [1989] baroclinic case to a mixed barotropic and baroclinic flow in a channeled, two-layer model (non-uniform velocity in the lower layer), and finds the possibly of a resonance between an upper-layer gravity wave and a lower-layer shear wave. The baroclinic, asymmetric centrifugal instability is examined by *Bouchut et al.* [2011] in a barotropic Bickley jet in a two-layer shallow-water model.

Several 3D instability problems were solved in a rotating, stratified barotropic flow: an elliptical flow with uniform potential vorticity [*McWilliams and Yavneh*, 1998], a centrifugally stable Taylor-Couette flow [*Molemaker et al.*, 2001, *Yavneh et al.*, 2001], a geostrophic boundary current with uniform potential vorticity [*McWilliams et al.*, 2004], and a horizontal plane couette flow [*Vanneste and Yavneh*, 2007]. All these studies identify the ageostrophic instabilities as a type of AAI, and their growth rates have an inverse exponential dependence on $Ro$. *de La Cruz-Heredia and Moore* [1999] find an ageostrophic, barotropic instability due to the coupling of a shear wave and a Kelvin wave in a bounded piecewise linear shear with a discontinuity. In the bounded barotropic flows [*de La Cruz-Heredia and Moore*, 1999, *McWilliams et al.*, 2004, *Molemaker et al.*, 2001, *Vanneste and Yavneh*, 2007, *Yavneh et al.*, 2001], at least one Kelvin wave is involved in the ageostrophic instability. The ageostrophic instability in an Eady flow (a baroclinic flow) is well understood from earlier studies [*Molemaker et al.*, 2005, *Nakamura*, 1988, *Plougonven et al.*, 2005, *Stone*, 1966]. It is interpreted as a coupling between an edge Rossby wave and a Doppler-shifted inertia-gravity wave. Its growth rate strongly increases near the neighborhood of $A - S = 0$, hence it is also identified as a type of AAI. An ageostrophic instability which couples topographic Rossby waves and inertia-gravity waves is found by *Sutyrin* [2008] in a stratified layer of fluid between two homogenous layers, with constant $A$ and $S$, and $A$-$S \neq 0$. To examine the instabilities in a stratified flow of a mixed barotropic and baroclinic type, *Moore and Peltier* [1987, 1990] and *Snyder* [1995] study a two-dimensional front with uniform potential vorticity, and are not able to find small-scale ageostrophic instabilities. *Yamazaki and Peltier* [2001a,b] revisit the problem by adding a small potential vorticity variation cross the front; they find several small-scale instabilities, but it is not clear whether the unstable modes were well resolved. *Barth* [1994] examines a thermal-wind balanced coastal jet (front) with a realistic stratification, and finds a surface-trapped, baroclinic, small-scale instability, the nature of which is yet unclear. Recently *Ménesguen et al.* [2012] study the ageostrophic instability in a stratified, interior jet with both barotropic and baroclinic shear, and find the characteristics of the unstable modes are transformed through a near-degeneracy in the neighborhood of $A - S = 0$.

### 1.2.3 Physical clarification of the $A - S$ condition

As mentioned in Sec. 1.1, the large-scale and mesoscale flows are within the constraints of "balanced" dynamics. It is strongly controlled by rotation and stable stratification, and is hydrostatic in vertical momentum and gradient-wind balanced in horizontal momentum (the horizontal diagnostic force balance is among Coriolis force, centrifugal force and pressure gradient force). This simplified fluid dynamical system is described by a set of Balanced Equations, which are a set of asymptotically consistent approximations built around the diagnostics of force balance in the larger scale motions. The Balanced Equations are not unique; for instance, the quasigeostrophic equations are one set of Balanced Equations with an accuracy of $O(Ro)$. Many Balanced Equations have been formulated [*Charney*, 1962, *Lorenz*, 1960], which have a higher accuracy of $O(Ro^2)$ than the quasigeostrophic model. As a partial differential equation system, the Balanced Equations do not have a solution in some particular parameter regime or flow configurations. For instance, in a gradient-wind balanced anticyclone, the pressure cannot have an extreme maximum. The solvability conditions show that there are singularities in the time integration of Balanced Equations when some critical conditions are satisfied anywhere in the domain. These critical conditions are called "limit of balance". Once beyond the conditions, the balanced time evolution would break down and the flows are no longer "balanced" and cannot be described by a balanced model. Furthermore, the unbalanced fluctuations would begin to evolve and grow; hence the limits for the time evolution of balanced model are very likely to relate with the onset conditions of unbalanced (ageostrophic) instabilities, which would not occur in Balanced

Equations and generate unbalanced fluctuation when the balanced time integration is broken down.

The solvability of a particular set of $O(Ro^2)$ Balanced Equations are analyzed by *McWilliams et al.* [1998] and three precise conditions for the limits of time integration of Balanced Equations are given. The solvability conditions must be satisfied in initial conditions and anytime in the time integration to keep the motions stay in the constraints of balance. The first two conditions ($N^2$ changes sign and $A$ changes sign) are consistently associated with two classic ageostrophic instabilities. The third condition, $A - S$ changes sign, is not familiar to us. $A - S$ must be positive in a balanced flow in order to be able to solve the gradient-wind balance equation for the horizontal streamfunction by inverting the operator of the Monge-Ampere equation with a nonzero divergence of the pressure gradient force on its right-hand side. Therefore, the $A - S$ sign change implies inability to time integrate the Balanced Equations, hence necessarily a growth of unbalanced flow. However, it is yet unclear how this relates to the linear instability problem for fluctuations about a balanced basic-state flow. We name the instability that is associated with this $A - S$ condition as an AAI. As mentioned in Sec. 1.2.2, several types of flow [*McWilliams and Yavneh*, 1998, *McWilliams et al.*, 2004, *Ménesguen et al.*, 2012, *Molemaker et al.*, 2001, 2005, *Yavneh et al.*, 2001] have been examined and AAI are found in those flows. Although all the AAI are not the same, two common points are found: 1) Not like the other two ageostrophic instabilities (GI and CI), the occurrence of AAI may be in the neighborhood of, rather than precisely at, $A - S = 0$; its growth rate vanishes as $Ro \rightarrow 0$ and strongly increases beyond the $Ro$ where $A - S = 0$; 2) Almost all the AAIs involve at least an inertia-gravity wave or a Kelvin wave coupled to the mean shear. These two characteristics are quite different from GI, CI or any other known 3D instability in stratified flows, which implies a new type of broadly existing instability. The theoretical prediction in *Molemaker et al.* [2001] and *Yavneh et al.* [2001] is validated by *Le Bars and Le Gal* [2007], who examine a stably stratified Taylor-Couette flow and observe the AAI in the form of non-axisymmetric oscillating modes. The modes do not exist in quasigeostrophic limit, and is non-centrifugal and non-gravitational. In their work, the instability appears when two vertically counter-traveling helicoidal waves superimpose and resonate. Perhaps more future lab experiments on different types of mean flow would help us for a full physical picture of the $A - S$ condition and AAI.

## 1.3 Objectives and Layout of This Dissertation

Most of the examined flows are special, simplified cases: the occurrence of an ageostrophic instability relies on the existence of boundaries, equator, surface outcropping, or singular potential vorticity, which support particular neutral mode types (e.g., boundary-trapped wave, Kelvin wave, frontal wave, singularity-trapped wave). Our work aims to study the generic characteristics of ageostrophic instability in more general mean flows (continuously differentiable interior flows $\overline{U}(y)$ and $\overline{U}(z)$ with a continuous, non-uniform potential vorticity, and without vertical and side boundaries or surface outcropping), which can provide us a comprehensive guide to understand the possible process for the loss of balance in the interior atmosphere and ocean. If we review the criteria of currently known linear instability conditions with increasing $Ro$ and $Fr$, the instabilities appear in the following order: barotropic or baroclinic instability (the only type that exists in the quasigeostrophic regime), anticyclonic, ageostrophic instability (AAI), centrifugal instability (CI), Kelvin-Helmholtz instability (KHI), and finally gravitational instability (GI) when the flow is unstably stratified. Our goal is to understand a general local route for the loss of balance within the control of rotation and stable stratification, so we are more interested in the ageostrophic instabilities that occur for an intermediate $Ro$ and $Fr$ (below the criteria for CI, KHI and GI). We solve the linear instability problem of an interior horizontal shear $\overline{U}(y)$ in a single-layer, $f$-plane shallow-water model, and that of an interior vertical shear $\overline{U}(z)$ in a $f$-plane, constant-stratification Boussinesq model.

The parallel mean flows we examine are idealized flows, while the real mesoscale eddies are more complicated vortices. The flows we study can be treated as cross-sections of vortices; the instability analysis of these simpler flows is easier to be solved hence can provide us a more complete view of all the possible instabilities. Although the behaviors of parallel flows and vortex flows are different, but the main conclusions such as the criterion for the instability, the dynamical mechanism would be similar. The mesoscale eddies have a typical length scale of 10 to 100 $km$, with a horizontal velocity scale 0.05 to 0.5 $m/s$, and a vertical velocity scale 0.01 $m/s$. Figure 1.2 shows an example of global distribution of mesoscale eddies by satellite data. The eddies are generated by the large-scale circulations through barotropic and baroclinic instabilities. If a mid-latitude eddy (where $f$ is typically $10^{-4}/s$) has a horizontal length of 10 $km$ and horizontal velocity of 0.5 $m/s$, the $Ro$ for this eddy would be 0.5. Our shear flows do not have a very large $Ro$, so they are still be able to represent the realistic regimes. A typical length scale for submesoscale flows is 1 $km$ and they have a large vertical velocity due to strong horizontal divergence (0.1 $m/s$ or larger), so we expect the resulted unstable fluctuations to have a much smaller horizontal scale compared to the mean shear. In the problems that we solve, the influence from the large-scale circulation ($\sim$ 1000 $km$) is not considered.

In the shallow water model, because there is no interior stratification and the horizontal velocity is depth-independent, the baroclinic (BCI), gravitational, centrifugal, and Kelvin-Helmholtz instabilities do not occur. In a 3D stratified flow, all those instabilities could exist if the onset condition is satisfied. With the linear instability analysis approach, the following questions are mainly addressed in our work: 1) What is the generic type of ageostrophic instability of an interior barotropic shear flow in a rotating shallow water fluid? 2) What is the generic type of ageostrophic instability of an interior baroclinic shear flow with $A$ (or $PV_{Ertel}$) $> 0$ in a rotating, stably stratified fluid? 3) How do the criteria of these instabilities relate to the theoretical frameworks discussed in Sec. 1.2.1? 4) What are the dynamical mechanisms for the ageostrophic instabili-

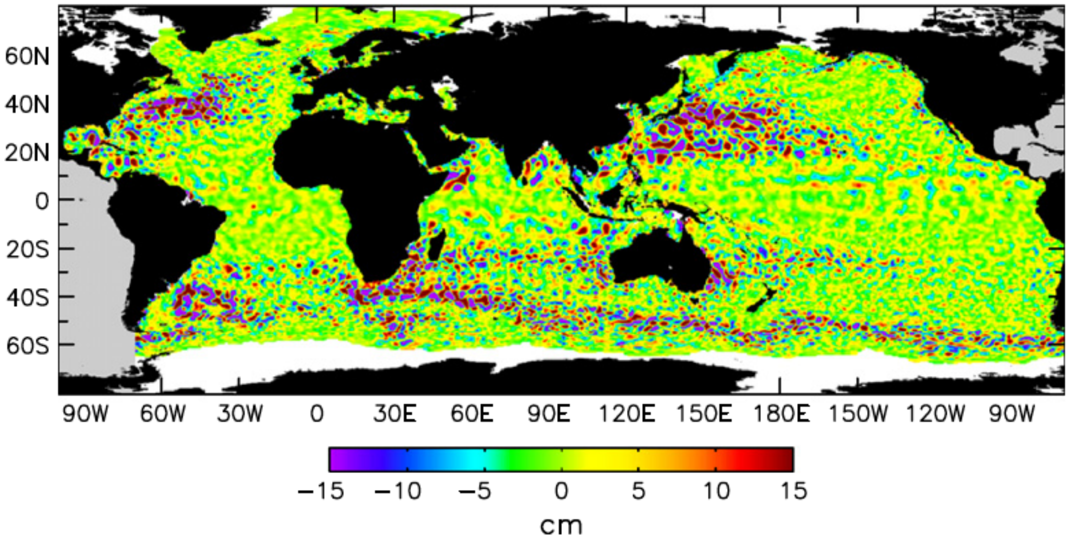

Figure 1.2: An example of global mesoscale eddy distributions (sea surface height field) on 28 August 1996 constructed from the merged T/P and ERS-1 data after spatially high-pass filtering with half-power filter cutoffs of $20^o$ of longitude by $10^o$ of latitude. Figure from *Chelton et al.* [2011].

ties? Is there a difference between a shallow-water or layered flow, and a continuously stratified flow?

In this Dissertation, Chapter 2 presents the study of ageostrophic instability in rotating shallow water equations, including general types of instability found in the mean flows (B-B, B-G and G-G), the criterion for their occurrence, associated dynamical mechanism, and a nonlinear example for the ageostrophic instability. The characteristics of two types of ageostrophic instability (AI1 and AI2) in a stratified, interior baroclinic shear flow in Boussinesq equations, including their physical mechanisms, *Ro* dependence, balance diagnostics, and energetics are demonstrated in Chapter 3. This dissertation is summarized with discussion and future questions in Chapter 4.

# CHAPTER 2

## Ageostrophic Instability in Rotating Shallow Water

This chapter solves the linear instability problem in a single-layer, uniformly-rotating (non-equatorial) shallow-water model for several balanced mean shear profiles $\overline{u}(y)$ with a continuous, non-uniform potential vorticity, and without side boundaries or vanishing layer depth. We are searching for the generic type of ageostrophic instability, the criterion for its occurrence, and the associated dynamical mechanism. Note that because there is no interior stratification and the horizontal velocity is depth-independent, the baroclinic, gravitational, centrifugal, and Kelvin-Helmholtz instabilities do not occur. Section 2.1 specifies the equations, the non-dimensional parameters, and the mean flows. A general picture for the neutral and unstable modes is shown in Sec. 2.2, followed by a detailed study for each type of instability in Sec. 2.3 and 2.4. Section 2.5 examines $Ro$ and $Fr$ dependence, the degree of ageostrophy, and the energy diagnostics for the instabilities. A nonlinear example of the ageostrophic instability is shown in Sec. 2.6. Sec. 2.7 is a brief summary of main conclusions.

## 2.1 Shallow Water Equations and Mean Flows

We study the instability problem in a $f$-plane rotating conservative shallow water model, with dimensional equations,

$$\begin{cases} \dfrac{\partial u}{\partial t} + u\dfrac{\partial u}{\partial x} + v\dfrac{\partial u}{\partial y} - fv + g'\dfrac{\partial h}{\partial x} = 0 \\ \dfrac{\partial v}{\partial t} + u\dfrac{\partial v}{\partial x} + v\dfrac{\partial v}{\partial y} + fu + g'\dfrac{\partial h}{\partial y} = 0 \\ \dfrac{\partial h}{\partial t} + \dfrac{\partial (uH)}{\partial x} + \dfrac{\partial (vH)}{\partial y} = 0 \quad , \end{cases} \tag{2.1}$$

where $f$ is the coriolis frequency, $g'$ is the reduced gravity, and $H = H_0 + h$ is the total water depth, with $H_0$ the average value. $h$ is the surface elevation, and $u$ and $v$ are zonal and meridional velocities, respectively. The equations can be non-dimensionalized to yield two independent parameters: Rossby number $Ro$ and Froude number $Fr$,

$$Ro = \frac{U_0}{fL}, \qquad Fr = \frac{U_0}{\sqrt{g'H_0}},$$

where $U_0$ is the velocity scale of the mean flow and $L$ is the horizontal scale of the mean shear. We decompose the variables into the mean parallel flow and the fluctuations:

$$u = \overline{u}(y) + u'(x,y,t)\,, \qquad v = v'(x,y,t)\,, \qquad h = \overline{h}(y) + h'(x,y,t).$$

The non-dimensional linearized fluctuation equations are

$$\begin{cases} Ro(\dfrac{\partial u'}{\partial t} + \overline{u}\dfrac{\partial u'}{\partial x} + v'\dfrac{\partial \overline{u}}{\partial y}) - v' + \dfrac{\partial h'}{\partial x} = 0 \\ Ro(\dfrac{\partial v'}{\partial t} + \overline{u}\dfrac{\partial v'}{\partial x}) + u' + \dfrac{\partial h'}{\partial y} = 0 \\ Fr^2(\dfrac{\partial h'}{\partial t} + \overline{u}\dfrac{\partial h'}{\partial x} + v'\dfrac{\partial \overline{h}}{\partial y}) + (Ro + Fr^2\overline{h})(\dfrac{\partial u'}{\partial x} + \dfrac{\partial v'}{\partial y}) = 0 \quad , \end{cases} \tag{2.2}$$

with the mean flow in geostrophic balance, $\overline{u} = -d\overline{h}/dy$. Assuming the solutions have a form $(u', v', h') = Re[(\hat{u}(y), \hat{v}(y), \hat{h}(y))e^{i(kx-\omega t)}]$ , where $k$ is the downstream ($x$-direction) wavenumber and $\omega$ is the wave frequency, then we have an eigenvalue problem:

$$\begin{aligned}&\begin{pmatrix} kRo\overline{u} & -i(Ro\frac{\partial\overline{u}}{\partial y}-1) & k \\ -i & kRo\overline{u} & -i\frac{\partial}{\partial y} \\ k(Ro+Fr^2\overline{h}) & -i(Fr^2\frac{\partial\overline{h}}{\partial y}+(Ro+Fr^2\overline{h})\frac{\partial}{\partial y}) & kFr^2\overline{u} \end{pmatrix}\begin{pmatrix} \hat{u} \\ \hat{v} \\ \hat{h} \end{pmatrix} \\ &= \omega\begin{pmatrix} Ro & 0 & 0 \\ 0 & Ro & 0 \\ 0 & 0 & Fr^2 \end{pmatrix}\begin{pmatrix} \hat{u} \\ \hat{v} \\ \hat{h} \end{pmatrix}.\end{aligned} \tag{2.3}$$

Note that all the mentioned variables will be non-dimensional henceforth.

We examine four types of mean flow: the Bickley jet ($j = 1$), the cyclonic and anticyclonic double jet ($j = 2$), the triple jet ($j = 3$), whose analytical forms are

$$\overline{u} = A_1 cosh^{-2} y \quad (j = 1), \tag{2.4}$$

$$\overline{u} = -A_2 y e^{-y^2} \quad \text{or} \quad \overline{u} = A_2 y e^{-y^2} \quad (j = 2), \tag{2.5}$$

$$\overline{u} = A_3(1-2y^2)e^{-y^2} \quad (j = 3), \tag{2.6}$$

respectively. $A_1$, $A_2$ and $A_3$ are positive constants. The value of $A_3$ is set such that $\overline{h}_{max} = 1$ in $j = 3$, and the $j = 1$ and 2 mean flows are normalized to have the same $\overline{u}_{max} - \overline{u}_{min}$ by adjusting the value of $A_1$ and $A_2$. The $\overline{u}(y)$ and $\overline{h}(y)$ mean profiles are shown in Fig. 2.1. The $j = 3$ mean flow is more general in the sense that it contains a Bickley jet in the center, an anticyclonic shear on the left, and a cyclonic shear on the right. The total water depth should be positive, which implies a limitation of the existence of the mean flow (that has $\overline{h}_{min} < 0$) in the ($Ro$, $Fr$) space. The condition $H = H_0 + \overline{h}^* > 0$ (where $^*$ denotes dimensional variables) implies $\frac{Fr^2}{Ro}\left|\overline{h}_{min}\right| \leqslant 1$, so the limitation condition is $Fr^2 \leqslant \lambda Ro$ for the mean flows. The value of $\lambda$ depends on the particular mean flow: $\lambda = 0.2968$ for $j = 1$, $\lambda = 0.5098$ for $j = 2$ cyclonic, and $\lambda = 1$ for $j = 3$. This limitation does not apply to the $j = 2$ anticyclonic shear, where it always satisfies $H = H_0 + \overline{h}^* > 0$. Fig. 2.2 shows the $\overline{q}(y)$ profiles of the mean flows for small

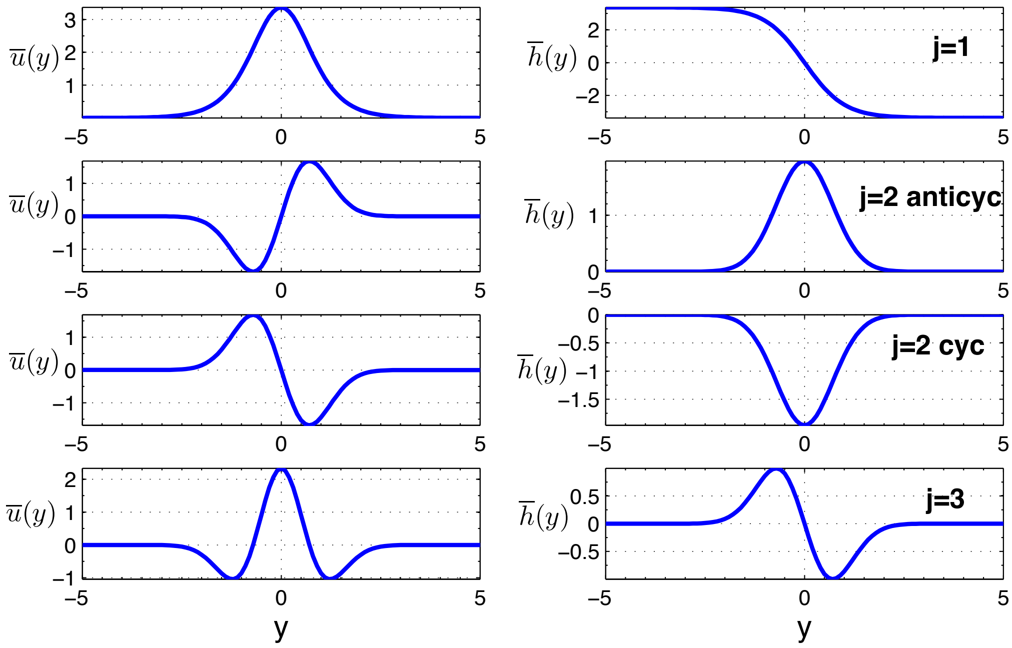

Figure 2.1: Mean velocity $\overline{u}(y)$ (left) and geostrophic-balanced surface elevation $\overline{h}(y)$ (right) for $j = 1$, 2 (anticyclonic), 2 (cyclonic) and 3, respectively. To normalize the mean flows, we choose $\overline{h}_{max} = 1$ in $j = 3$, and all the mean flows have the same $\overline{u}_{max} - \overline{u}_{min}$ value.

(left) and moderate (right) $Ro$, where

$$\overline{q} = \frac{1 - Ro\overline{u}_y}{1 + \frac{Fr^2}{Ro}\overline{h}} \,. \tag{2.7}$$

For small $Ro$ and $Fr$ (quasi-geostrophic regime), the water depth is nearly constant in $y$. The magnitude of $\overline{q}$ is symmetric for the regions with $\overline{h} > 0$ and $\overline{h} < 0$, and its value is small. For moderate $Ro$ and $Fr$, the surface elevation becomes comparable to the average water depth. $\overline{h} > 0$ has a small effect on $\overline{q}$ (Fig. 2.2 (f)), while in the $\overline{h} < 0$ region, $\overline{q}$ has a large value due to the thin water depth (Fig. 2.2 (e), (g) and (h)). For a fixed $Ro$, increasing $Fr$ leads to a significant increase of the local $\overline{q}$ in the $\overline{h} < 0$ region (not shown).

It has been identified that three types of solution coexist in a $\overline{u}(y)$ flow: the conjugate

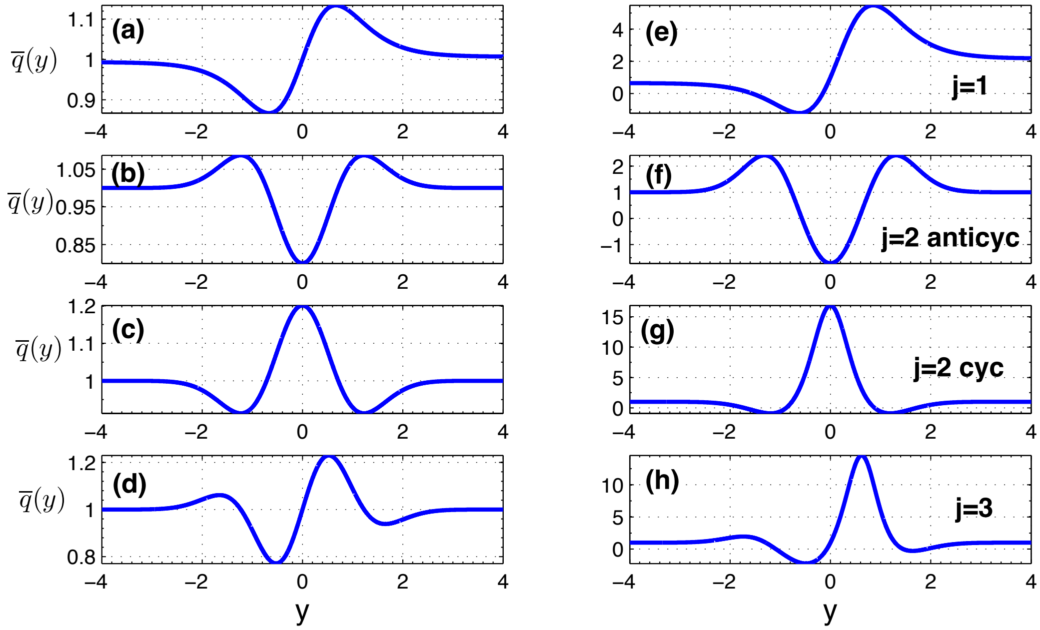

Figure 2.2: Mean potential vorticity $\overline{q}(y)$ for $j = 1$, 2 (anticyclonic), 2 (cyclonic) and 3, respectively (from top to bottom). The small *Ro* (= 0.05) profiles are shown on the left, and the finite *Ro* (= 1) profiles are shown on the right. In (a), (b), (c) and (d), $Ro = 0.05$ and $Fr = 0.01$. In (e), $Ro = 1$ and $Fr = 0.4$. In (f) and (g), $Ro = 1$ and $Fr = 0.6$. In (h), $Ro = 1$ and $Fr = 0.8$.

pairs of growing and decaying modes, the non-singular neutral mode, and the singular continuum mode [*Held*, 1985, *Lin*, 1961]. In shallow water equations, the eigenvalue problem can be expressed by $A\phi = \omega B\phi$, where $A$ and $B$ are real matrices,

$$A = \begin{pmatrix} kRo\overline{u} & -(Ro\frac{\partial \overline{u}}{\partial y} - 1) & k \\ 1 & kRo\overline{u} & \frac{\partial}{\partial y} \\ k(Ro + Fr^2\overline{h}) & -(Fr^2\frac{\partial \overline{h}}{\partial y} + (Ro + Fr^2\overline{h})\frac{\partial}{\partial y}) & kFr^2\overline{u} \end{pmatrix},$$

$$B = \begin{pmatrix} Ro & 0 & 0 \\ 0 & Ro & 0 \\ 0 & 0 & Fr^2 \end{pmatrix},$$

and $\phi = \begin{pmatrix} \hat{u} & i\hat{v} & \hat{h} \end{pmatrix}^T$, with $^T$ meaning transpose. If $\omega$ and $\phi$ are its eigenvalue and eigenfunction, then according to $(A\phi)^* = A\phi^* = (\omega B\phi)^* = \omega^* B\phi^*$, $\omega^*$ and $\phi^*$ are also its eigenvalue and associated eigenfunction, where $^*$ means complex conjugate. Therefore, the growing and decaying modes appear in pairs in the non-viscous case. For the $j = 2$ mean flows, another symmetry appears because $\overline{u}(y) = -\overline{u}(-y)$ and $\overline{h}(y) = \overline{h}(-y)$. We have $A(y)\phi = \omega B\phi$, where $\phi = \begin{pmatrix} \hat{u}(y) & i\hat{v}(y) & \hat{h}(y) \end{pmatrix}^T$. Let $y \to -y$ and take the conjugate of the whole equation, it follows $A(y)\tilde{\phi} = (-\omega^*)B\tilde{\phi}$, where $\tilde{\phi} = \begin{pmatrix} \hat{u}^*(-y) & -i\hat{v}^*(-y) & -\hat{h}^*(-y) \end{pmatrix}^T$. A new symmetric eigenvalue $-\omega^*$ and associated eigenfunction are obtained. This means that the growing (or decaying) modes can be found in pairs ($\omega$ and $-\omega^*$), with the same growth rate and opposite-signed phase speeds, and their associated eigenfunctions $\phi$ and $\tilde{\phi}$ are partially symmetric and partially anti-symmetric in $y$. The paired unstable modes in $j = 2$ flows will be shown in Sec. 2.2. Besides the growing and decaying pairs, neutral mode solutions also exist for the equations, which can become unstable when they couple and interact (Sec. 2.2).

To solve the eigenvalue problem, we use an eigensolver with a Fortran library ARPACK. Because a large resolution is needed for an accurate solution, it is too expensive to compute the full-spectrum eigenvalues. ARPACK computes a few eigenvalues and corresponding eigenfunctions close to the given "target" (guessed eigenvalue) by a iterative convergence process. The result is checked with a linear time integration code. We discretize the differential operators by a second-order centered finite-difference method, in a staggered grid, with a resolution of $N \sim 5000$ in the $y$ direction. The domain in the computation is sufficiently large ([-5 5]) to remove the boundary influence on the unstable modes, which are trapped in the mean shear region. The boundary condition at $y = \pm 5$ is chosen to be $v' = 0$ and $\frac{\partial u'}{\partial y} = \frac{\partial h'}{\partial y} = 0$. We do not look for radiating instabilities by setting a matching boundary condition, therefore none of the unstable modes found by our eigensolver propagate along $y$. We check our result by increasing resolution in both grids and $k$ until the eigenvalue converges and no longer changes with higher resolution. The eigenvalues converge well for our current resolution. For most of our numerical results, viscosity terms ($Ek\nabla^2 u$, $Ek\nabla^2 v$) are not needed ($Ek$ is the Ekman number). However, there is a viscosity option in order to eliminate the unreliable eigenmodes that are marginally resolved. Some weakly unstable or neutral modes with critical layers could be inaccurately determined without viscosity. On the contrary, the unstable mode, which is our focus, has an imaginary part in the eigenvalue so it can be accurately calculated by the eigensolver. We have tested different $Ek$ values to make sure that the viscosity is sufficiently small that it has neglectable effect on the unstable modes. The correctness of our eigensolver is confirmed by reproducing the growth rate of the barotropic instability in a Bickley jet (Fig. 2 and 3 in *Poulin and Flierl* [2003] and Fig. 2 in *Lambaerts et al.* [2011]).

## 2.2 Neutral and Unstable Modes

The dynamical mechanism of instability has been commonly interpreted as a resonant coupling of two neutral waves in previous literature [*Gula and Zeitlin*, 2010, *Hayashi and Young*, 1987, *Sakai*, 1989]. In the general cases we investegate, this interpretation is helpful for us to understand the unstable modes, especially the ageostrophic modes, so this conventional concept is kept in this paper. The neutral wave modes are Doppler-shifted and modified by the background mean shear, with both frequency and mode structure being changed. When two neutral wave modes have the same frequency, they can interact and resonate with each other, leading to an instability.

### 2.2.1 Neutral Modes

In rotating shallow water equations, there are mainly two types of non-singular neutral wave modes in an interior shear flow that does not have side boundaries or surface outcropping: the shear wave mode and the inertia-gravity wave mode. The shear wave mode (also called "Rossby wave" or "vortical wave") is defined as the mode that exists due to the potential vorticity gradient. It is a balanced mode, which can be found in the quasi-geostrophic equations. For a finite $Ro$ where quasi-geostrophy fails, the shear wave mode may satisfy a higher-order balanced dynamics (Sec. 1.1). We refer to the balanced shear wave mode as the B mode.

To estimate the phase speed of the shear wave, we start from the $f$-plane quasi-geostrophic free-surface potential vorticity equation,

$$\frac{Dq_{QG}}{Dt} = 0\,, \qquad q_{QG} = \nabla^2\psi - \frac{Fr^2}{Ro^2}\psi\,, \tag{2.8}$$

where $\psi$ is the stream function with $\vec{u} = \hat{z} \times \nabla\psi$. The quasi-geostrophic potential vorticity equation follows from (2.1), by taking $Ro$ and $Fr$ to zero limit as their ratio remains a constant. The linearized potential vorticity equation is

$$(\frac{\partial}{\partial t} + \overline{u}\frac{\partial}{\partial x})(\nabla^2\psi' - \frac{Fr^2}{Ro^2}\psi') + \frac{\partial\psi'}{\partial x}(\frac{Fr^2}{Ro^2}\overline{u} - \overline{u}_{yy}) = 0\,. \tag{2.9}$$

With the assumption $\psi' = Re[\,\Psi(y)e^{i(kx-\omega t)}\,]$, we get

$$\Psi_{yy} + [\frac{d\overline{q}_{QG}/dy}{\overline{u} - c} - (k^2 + \frac{Fr^2}{Ro^2})]\Psi = 0\,, \qquad \frac{d\overline{q}_{QG}}{dy} = \frac{Fr^2}{Ro^2}\overline{u} - \overline{u}_{yy}\,. \tag{2.10}$$

To make a local estimate for the neutral mode, we assume $\frac{d\overline{q}_{QG}}{dy}$ and $\overline{u}$ are constant at local $y$, and hence $\Psi(y)$ has a form of $e^{ily}$. Then the estimated phase speed for the balanced shear wave mode becomes

$$C_{QG} = \overline{u} - \frac{d\overline{q}_{QG}/dy}{k^2 + l^2 + \frac{Fr^2}{Ro^2}}\,. \tag{2.11}$$

The locally estimated phase speed of the shear wave shows that beyond the Doppler shift of the mean velocity, its sign is opposite to the sign of the potential vorticity gradient. The mathematical expression of the phase speed becomes complicated with a finite *Ro* effect, but we expect its dependence on $\overline{u}$ and $\overline{q}_y$ qualitatively remains the same for the B mode, where

$$\frac{d\overline{q}}{dy} = \frac{\frac{Fr^2}{Ro}\overline{u}\,\overline{q} - Ro\overline{u}_{yy}}{1 + \frac{Fr^2}{Ro}\overline{h}}.$$

The background $\overline{q}_y$ is essential for the existence of the shear wave mode. With uniform potential vorticity [*Hayashi and Young*, 1987, *Satomura*, 1980], there is no instability that involves a B mode. For a fixed set of ($k$, $Ro$, $Fr$), a singular $\overline{q}_y$ value supports a single shear wave mode. In *Boss et al.* [1996] and *Dritschel and Vanneste* [2006], the stepwise uniform potential vorticity creates a singular $\overline{q}_y$ at the front, which supports a B mode trapped near the singular point. In *Killworth et al.* [1984], *Kubokawa* [1986] and *Gula and Zeitlin* [2010], the surface outcropping point is singular in $\overline{q}_y$ and supports a frontal-trapped wave, which behaves the same as a B mode at small wavenumbers. If $\overline{q}_y$ is continuous in $y$, a set of shear wave modes with a continuous range of phase speeds coexist due to the variation of $\overline{q}_y$. Belonging to balanced dynamics, the shear wave mode has a slow phase speed comparable to $\overline{u}$ when *Ro* is small.

Another type of non-singular neutral mode in rotating shallow water equations is the inertia-gravity wave mode. The inertia-gravity wave velocity is highly divergent, and hence it does not exist in the quasi-geostrophic regime. The mode is unbalanced, so any instability involving this mode is an unbalanced instability. We refer to the inertia-gravity mode as the G mode. The G mode has two branches: the P mode (positive phase speed branch, red dashed lines in Fig. 2.3) and the N mode (negative phase speed branch, blue solid lines in Fig. 2.3). Without mean flow background, the dispersion relation for an inertia-gravity wave mode is

$$C_p^{\pm} = \pm\sqrt{\frac{k^2 + l^2}{Fr^2} + \frac{1}{Ro^2}}\Bigg/ k\,, \tag{2.12}$$

where $l$ is the wavenumber in the $y$ direction, and $C_p^+$ ($C_p^-$) is the phase speed for the P (N) mode without mean flow. The inertia-gravity wave mode has a fast phase speed when $Ro$, $Fr << 1$. Without $\overline{u}(y)$, the phase speed of a neutral B mode and that of a neutral G mode are well separated. The Doppler shift and modification by $\overline{u}(y)$ lead to a possibility of an interaction between them.

### 2.2.2 Unstable Modes

We find three types of unstable mode in the mean flows: B-B, B-G and G-G instability. As mentioned in Sec. 2.2.1, the instabilities can be interpreted as a coupling between two neutral wave modes, so we name an instability by its resonating components. The B-B instability is the classical shear instability (barotrophic instability). The B-G and G-G instabilities are two different types of ageostrophic instability. An unstable B-G mode exists at small and intermediate $k$ (~1-5), with attributes of both a balanced shear wave mode, and an inertia-gravity wave mode. An unstable G-G mode exists at both intermediate and large $k$ (>3), with attributes of two inertia-gravity wave modes modified by $\overline{u}(y)$.

The growth rate $\sigma$ and downstream (i.e., in the $x$ direction) phase speed $C_p$ versus $k$ for the four mean flows are shown in Fig. 2.3-2.6. The results shown in the figures are for moderate $Ro$ and $Fr$ (order 1). The triple jet is the most general one among the mean flows, and all three types of instability appear in this mean flow. It provides us a complete view for the instabilities for a moderate $Ro$ and $Fr$, so the unstable modes of the triple jet are shown in the beginning and most of our further results are demonstrated in the triple jet. In Fig. 2.3, the black curves represent the B-B instability. The red dashed (P mode) and blue solid (N mode) curves are G modes. We label the G modes by P (or N) and the approximate wavenumber in $y$ (here we use a notation $m$ for these discrete wavenumbers), which only have integer or half integer values. At small and intermediate $k$ (~1-5), the unstable red or blue modes have a smooth growth rate over a broad $k$ band. They are a B-G instability. Although the green modes belong to neither a P nor an N group, they are also a B-G instability. The unstable modes with multiple growth rate peaks at intermediate and large $k$, where the P and N modes overlap, are a G-G instability. Figure 2.4 to 2.6 follow the same plotting convention as Fig. 2.3. Note that the $y$ axes of the growth rate plots in Fig. 2.3, 2.5 and 2.6 are of different scales. The G-G instability is somewhat weaker than the B-B and B-G instabilities; however, its occurrence extends to very large downstream wavenumbers, and the number of the unstable G-G modes is infinite (only a few examples are shown in Fig. 2.3 and 2.4). In sum, both B-G and G-G modes are unbalanced modes; the former has a board band in $k$ while the latter appears as peaks in growth rate.

B-B and B-G instabilities appear in all four types of mean flow. For moderate $Ro$ and $Fr$ (order 1), G-G instability only occurs in $j = 2$ (cyclonic) and $j = 3$ mean flows (shown in Fig. 2.3 and 2.4). We do find G-G instability in $j = 2$ (anticyclonic), but for very large $Ro$ (about 10). For $j = 1$, the G-G instability does not exist. As shown in Fig. 2.3, the balanced and ageostrophic instabilities have comparable growth rate in $j = 3$. With the same bulk $Ro = 1.0$ and $Fr = 0.7$, in $j = 2$ (cyclonic), the ageostrophic instability is dominant over the balanced one (Fig. 2.4), while in $j = 2$ (anticyclonic), the balanced instability is dominant (Fig. 2.5). The ageostrophic instability is weak in the Bickley jet even for a $Ro = 3.0$ (Fig. 2.6). As discussed in Sec. 2.1, the growth rate and dispersion curves occur in symmetric pairs for $j = 2$ (Fig. 2.4 and 2.5): the $P_m$ and $N_m$ modes have the same $\sigma(k)$ curve, and their $C_p(k)$ curves are symmetric around $C_p = 0$. Their corresponding eigenfunctions are symmetric ($v'$ and $h'$) or anti-symmetric ($u'$) about $y = 0$.

## 2.3 B-B Instability

The balanced (barotropic) instability [*Drazin and Reid*, 1981, *Poulin and Flierl*, 2003] is associated with the inflexion point in the parallel mean flow, where the potential vorticity gradient changes sign [*Rayleigh*, 1880]. This instability appears at small $k$ ($k < 2$).

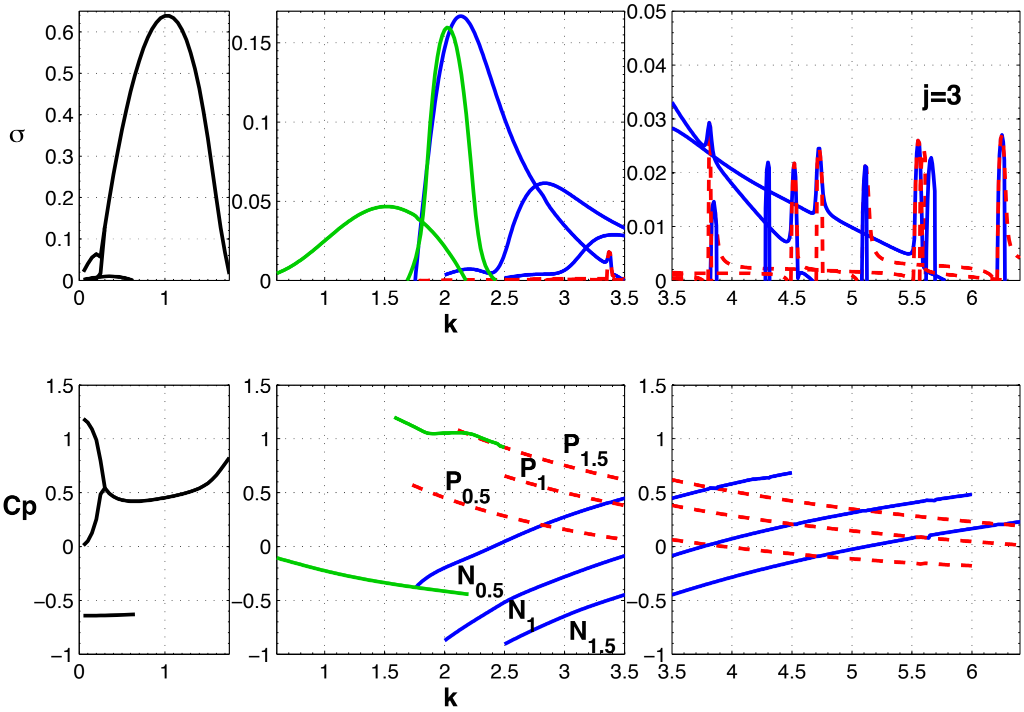

Figure 2.3: The growth rate $\sigma$ (upper) and phase speed $C_p$ (lower) for $Ro$ = 1.0, $Fr$ = 0.99 and $j$ = 3. The black lines represent B-B modes (left). The blue solid and red dashed curves represent N and P inertia-gravity wave modes respectively. The numbers next to N or P in the legend are integers or half integers, which denotes the wavenumbers in $y$. Following the N or P mode curves, the smooth $\sigma$ over a wide $k$ range presents B-G modes (middle). The green lines are also B-G modes (middle). The $\sigma$ peaks at intermediate and large $k$, where N and P modes overlap, are G-G modes (in the right plot). All the unstable B-B and B-G modes are shown in the plot, while only a few G-G modes are presented.

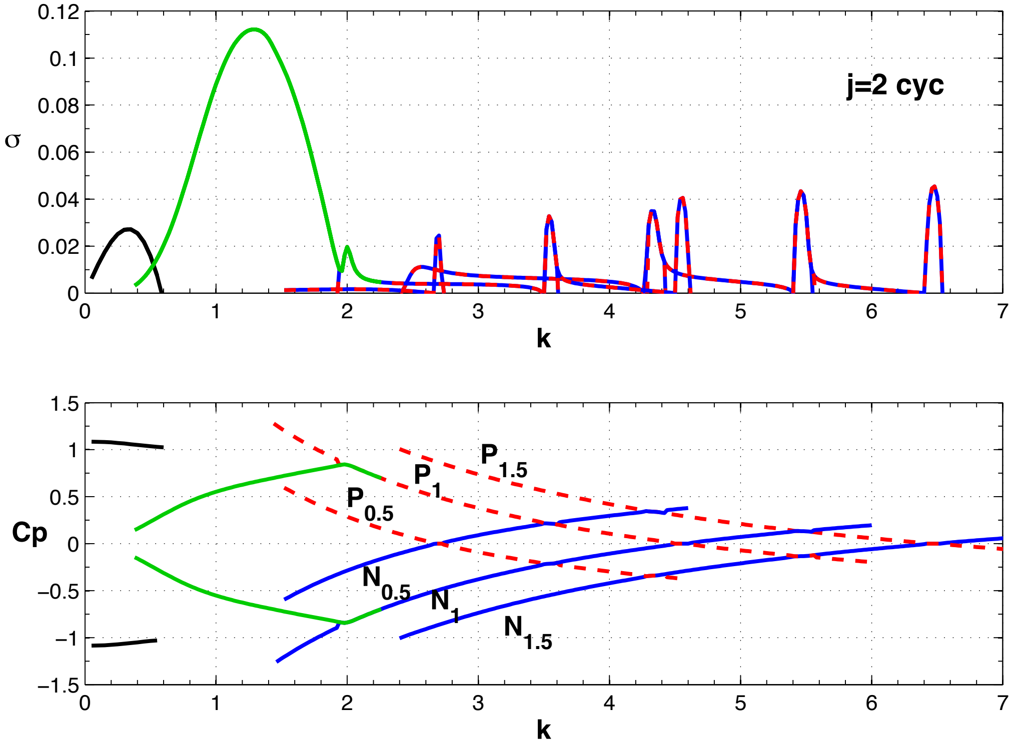

Figure 2.4: The growth rate $\sigma$ (upper) and phase speed $C_p$ (lower) plots for $Ro = 1.0$, $Fr = 0.7$ and $j = 2$ (cyclonic). Plotting conventions are the same as in Fig. 2.3. The plots contain B-B, B-G and G-G modes.

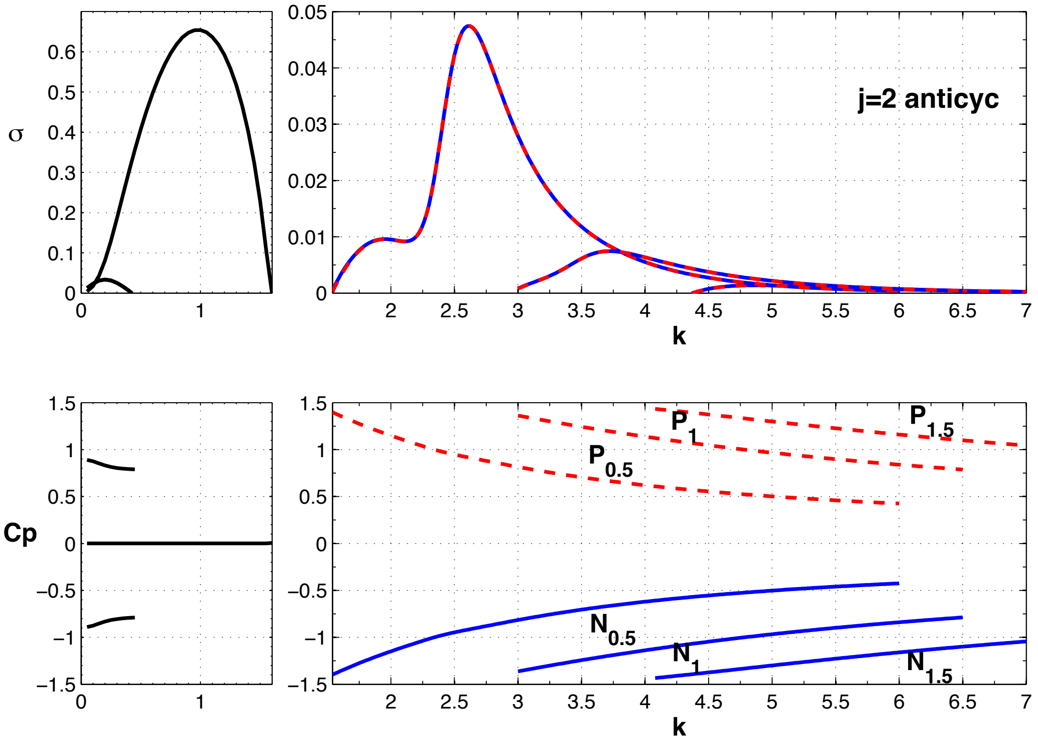

Figure 2.5: The growth rate $\sigma$ (upper) and phase speed $C_p$ (lower) plots for $Ro = 1.0$, $Fr = 0.7$ and $j = 2$ (anticyclonic). Plotting conventions are the same as in Fig. 2.3. The plots contain B-B (left) and B-G (right) modes.

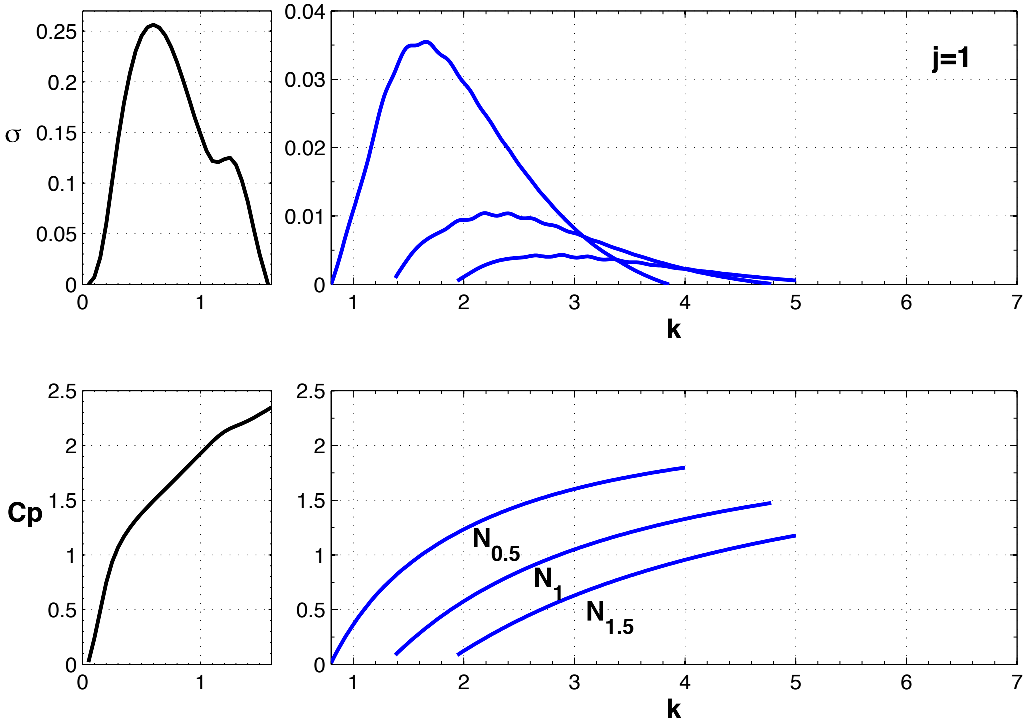

Figure 2.6: The growth rate $\sigma$ (upper) and phase speed $C_p$ (lower) plots for $Ro = 3.0$, $Fr = 0.9$ and $j = 1$. Plotting conventions are the same as in Fig. 2.3. The plots contain B-B (left) and B-G (right) modes.

The growth rate is the strongest at the $Fr = 0$ limit, where it is independent of *Ro*, and the increasing $Fr$ tends to suppress the B-B instability. Figure 2.7 shows the fluctuation fields of the balanced modes at a given time, for small (upper) and intermediate (lower) (*Ro*, $Fr$) pairs, and $j = 3$. The associated mean flow $\overline{q}_y$ profiles are shown below the fluctuation plots. For small (*Ro*, $Fr$), which is in the quasi-geostrophic regime, the field patterns are strongly geostrophic-balanced and quite symmetric in $y$. When (*Ro*, $Fr$) increases, the patterns are still mostly geostrophic. However, the fluctuations are no longer symmetric in $y$, and are mostly concentrated in the anticyclonic shear region. The magnitude of $\overline{q}_y$ becomes significantly large in the cyclonic shear region due to a strong surface depression. With a finite *Ro* and $Fr$ effect, the instability of a parallel cyclonic shear weakens much more significantly than that of an anticyclonic shear (Fig. 2.4 and 2.5). Therefore for moderate *Ro* and $Fr$, the B-B mode in $j = 3$ occurs only in the anticyclonic shear. The study of *Perret et al.* [2011] also shows that B-B instability favors the anticyclonic shear. The B-B instability is mostly balanced, even for an intermediate *Ro* and $Fr$.

The B-B instability can be interpreted as a resonance between two oppositely propagating shear wave modes. The shear wave mode in $\overline{q}_y > 0$ region has a negative phase speed, and the shear wave mode in $\overline{q}_y < 0$ region has a positive phase speed. With the Doppler shift of the mean flow velocity, the two B modes have the same phase speed and could interact with each other. The occurrence of the instability requires that the flow has both $\overline{q}_y > 0$ and $\overline{q}_y < 0$ regions, which is consistent with Rayleigh's condition.

We see multiple B-B modes for the mean flows. In $j = 3$, there are mainly three unstable B-B modes in the quasi-geostrophic regime. As *Ro* and $Fr$ increases, the growth rate of a B-B mode decreases. For $Ro = 1.0$ and $Fr = 0.99$ (Fig.2.3), two of the unstable B-B modes almost vanish, and only the strongest mode remains (the lower plot in Fig.2.7). In $j = 1$ and 2, there are two unstable B-B modes in the small-*Ro* limit (The two modes in $j = 1$ is also seen in *Lambaerts et al.* [2011]). For the *Ro* and $Fr$ shown in Fig. 2.6, the small growth rate B-B mode no longer exists in $j = 1$. With the

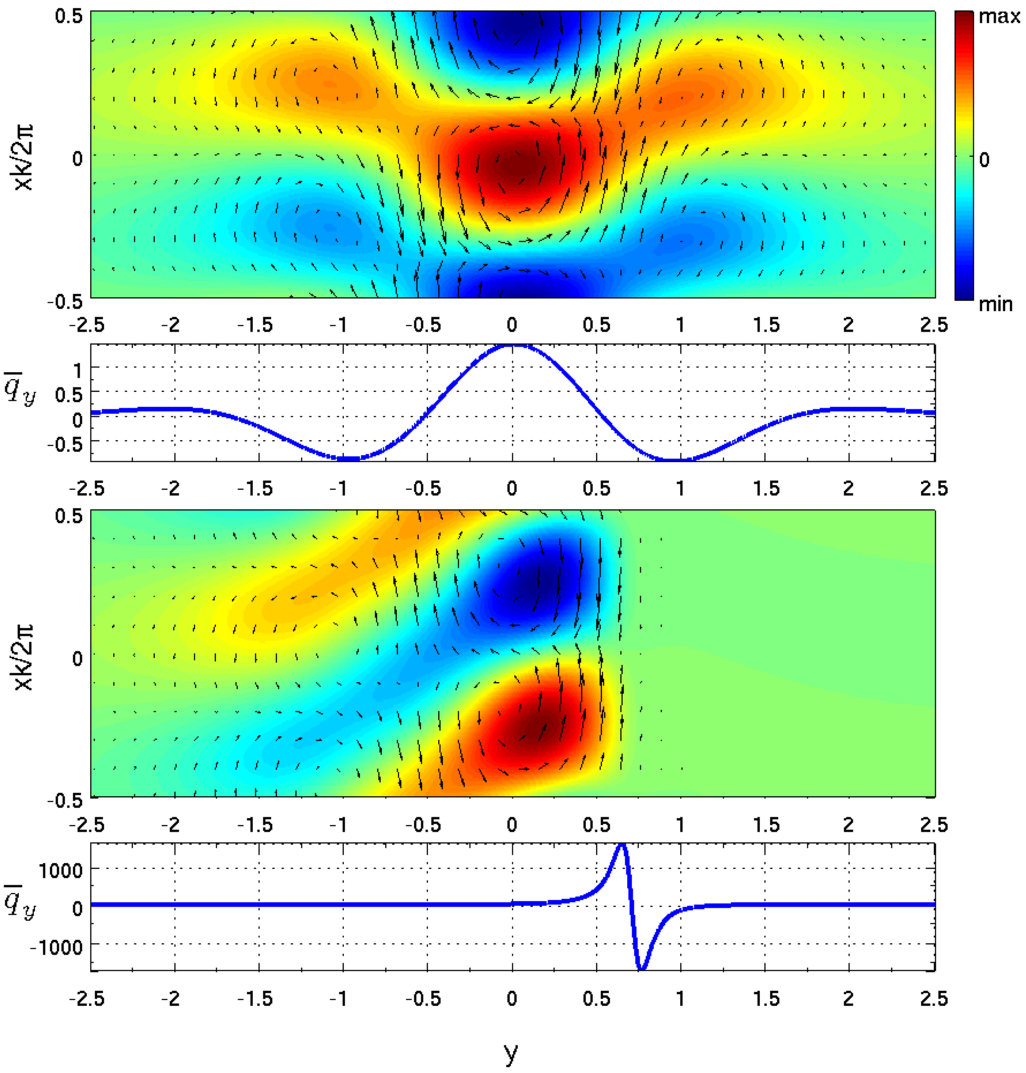

Figure 2.7: The fluctuation fields of the B-B modes at $k = 1$ and the mean potential vorticity gradient $\overline{q}_y$ profiles for $Ro = 0.1$, $Fr = 0.05$ (upper) and $Ro = 1.0$, $Fr = 0.99$ (lower) in $j = 3$. $h'$ is shown by the color; $u'$ and $v'$ are shown by the black vector arrows. For $h'$, red implies positive, blue implies negative and green implies zero. The same color code applies to all the color plots of $h'$ in subsequent figures.

same finite $Ro$ and $Fr$, both unstable B-B modes remain in the anticyclonic shear (Fig. 2.5) while only one remains with a very weak growth rate in the cyclonic shear (Fig. 2.4).

## 2.4 G-G and B-G Instabilities

The G-G and B-G modes are unbalanced instabilities. Figure 2.8 shows an example of the fluctuation fields for the two types of mode in $j = 3$. The fluctuations have an inertia-gravity wave mode pattern in $y$ for both types. All G-G and B-G unstable modes have critical layers (shown by the black straight lines in Fig. 2.8). For a G-G mode, there are two G components, distributed on each side of the critical layer. Only one G component appears in a B-G mode.

The G-G instability can be interpreted as a sharp resonance between two inertia-gravity wave modes from each group (N and P) respectively. The analytical dispersion relation for a G mode without the mean flow in shown in (2.2.1). With the existence of a mean flow background, dispersion relation curves are modified. Because the mean flow varies slowly, we assume the solution has a form $e^{ily}$ in $y$ to make a local estimation of the new dispersion relation for the two groups of G modes:

$$\hat{C_p}^{\pm} = \overline{u}^{\pm} \pm \sqrt{(k^2 + m^2)(\frac{1}{Fr^2} + \frac{\overline{h}^{\pm}}{Ro}) + \frac{1}{Ro^2}}\Big/ k \ , \tag{2.13}$$

where $\overline{u}^{+}$ or $\overline{u}^{-}$ is the local mean flow velocity, and $\overline{h}^{+}$ or $\overline{h}^{-}$ is the associated local surface elevation. The values of $\overline{u}^{+}$, $\overline{u}^{-}$, $\overline{h}^{+}$, and $\overline{h}^{-}$ are constants, which can be obtained by averaging the $\overline{u}$ or $\overline{h}$ over the $y$ region where the G component is located. Note that the meridional wavenumber is represented by $m$ in this new dispersion relation. Without the mean flow, the meridional wavenumber $l$ is continuous, while with the mean flow, only integer and half integer meridional wavenumbers are allowed, so we change to the notation $m$. Four $C_p$ curves of each group (in red and blue, respectively) calculated from (2.2.1) are shown in Fig. 2.9(a). They are the dispersion curves for

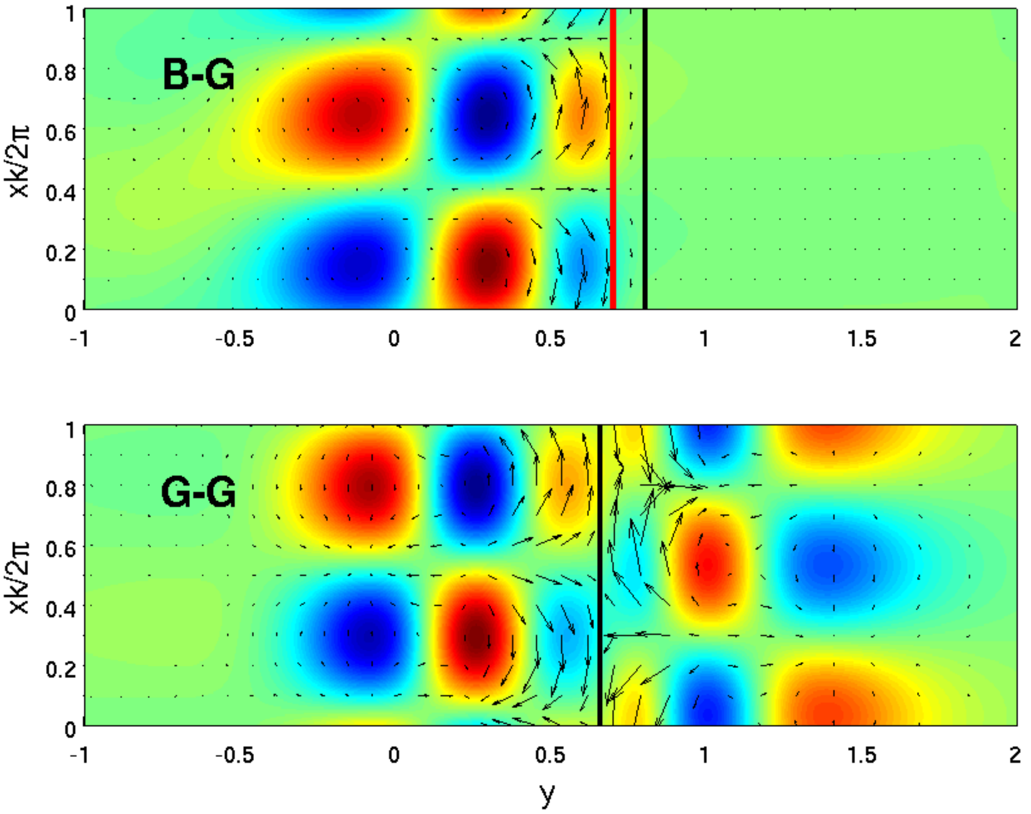

Figure 2.8: The fluctuation fields of a B-G mode at $k = 2.83$ (upper) and a G-G mode at $k = 4.52$ (lower) for $Ro = 1.0$, $Fr = 0.99$ and $j = 3$. $h'$ is shown by the color; $u'$ and $v'$ are shown by the black vector arrows. The straight black line indicates the critical layer where $\overline{u} = Cp$, and the straight red line indicates the inflection point where $\overline{q}_y = 0$.

the free G modes without the mean flow. Figure 2.9(b) shows the mean flow and the fluctuation $h'$ for a resonant G-G mode in $j = 3$, as a function of $y$. The fluctuation has two G components: the left one ($y < 0.8$), in the N group, is concentrated in the positive-signed $\overline{u}$ region, and the right one ($y > 0.8$), in the P group, is concentrated in the negative-signed $\overline{u}$ region. With the Doppler shift and modification by the mean flow, the P group is negatively shifted and the N group is positively shifted, leading to a cross of a pair of G mode $C_p$ curves. When the two G modes have the same phase speed, they can resonate with each other, and instability occurs. The $\hat{C_p}^+$ and $\hat{C_p}^-$ estimated from (2.13) are shown in Fig. 2.9(c). They are well consistent with the $C_p$ obtained by the eigensolver in Fig. 2.9(d). Figure 2.10 shows an example of the G-G resonance. The two plots on the left column are the growth rate and phase speed curves, zoomed in the $P_2$-$N_2$ resonant peak region. The right column shows the fluctuation $h'$ of the unstable resonant mode (A) and its component G modes (B and C), respectively. When the $C_p$ curves separate, the two G modes are almost stable, and only one G mode appears in the fluctuation pattern. When the curves overlap, the growth rate appears as a peak and the fluctuation pattern contains both G components.

Rather than having a sharp resonant peak in the growth rate, the B-G modes occur over a wide $k$ range in between the B-B modes and the G-G modes. We interpret an unstable B-G mode as a result of the interaction between a B mode and a G mode. The fluctuation of the unstable mode is highly ageostrophic, and its growth rate vanishes for a small $Ro$ and $Fr$. The G component appears in the $y$ region where the local $\overline{u}$ is opposite-signed to the phase speed of the free neutral G mode. As discussed in Sec. 2.2, the neutral G mode is a fast mode and the neutral B mode is a slow mode; they are well separated without the background mean flow. With the Doppler shift of the mean flow and a finite $Ro$ and $Fr$, the phase speed of the G mode becomes small, and thus possible to interact with a slow B mode. Because all our mean flows have continuous, non-uniform $\overline{q}_y$, many B modes within a continuous range of phase speed values coexist and might resonate with the G mode. Therefore, we cannot identify a particular B

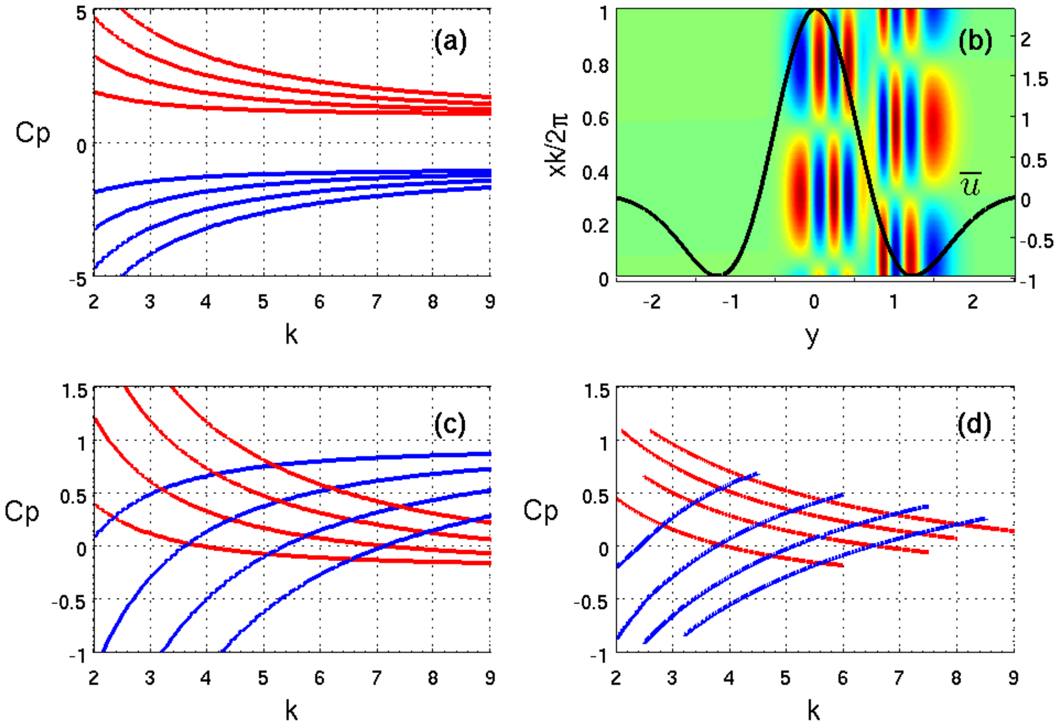

Figure 2.9: An explanation of the G-G resonance by $C_p$ for $Ro$ = 1.0, $Fr$ = 0.99 and $j$ = 3. (a) shows the $C_p$ curves of a few neutral G modes without mean flow. (b) is the fluctuation $h'$ (in color) of a G-G mode at $k$ = 8.01, with the background mean flow superimposed (black curve, right axis). (c) shows the $C_p$ curves with the modification by the local mean flow calculated from (2.13) (see text). (d) shows the same $C_p$ curves as (c), except that they are obtained from the numerical eigensolver.

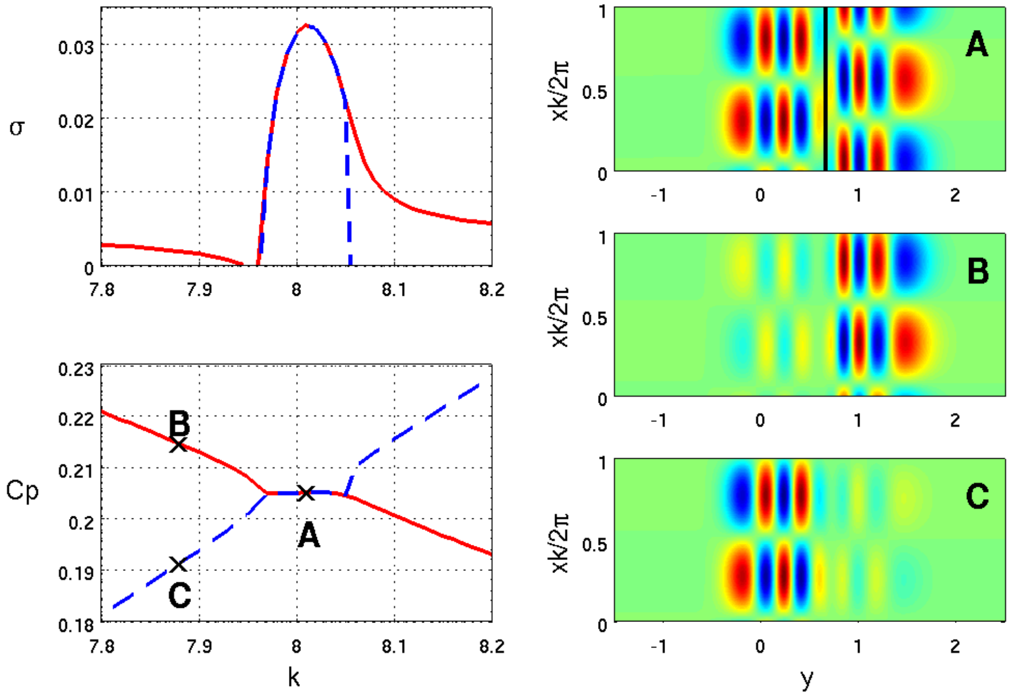

Figure 2.10: Fluctuations *h*′ (right column) for an unstable G-G mode ($P_2$-$N_2$) (A) at *k* = 8.01 (with the black line indicating the critical layer) and its neighboring component G modes: a weakly unstable $P_2$ mode (B) and a neutral $N_2$ mode (C) at *k* = 7.88, for *Ro* = 1.0, *Fr* = 0.99, and *j* = 3. The left column shows the zoomed-in growth rate and phase speed curves around *k* = 8.01.

component (in contrast to the G component in B-G and G-G instabilities). The pattern imprint of the G component is clear while that of the B component is obscure in the eigenfunctions for a large growth rate B-G mode (Fig. 2.8), though we do see the imprint of the B component in weakly unstable B-G modes (not shown), where the coupling of the B and G modes is not strong. For special shallow-water flows with a singular $\overline{q}_y$ [*Boss et al.*, 1996, *Dritschel and Vanneste*, 2006, *Gula and Zeitlin*, 2010, *Kubokawa*, 1986], the B component is a distinct mode and has an identifiable pattern imprint trapped near the singular point. However, with our continuous, smooth $\overline{q}_y$, the B component is less evident in the unstable mode. The obscurity of B component is also found in *Balmforth* [1999] in a flow without rotation. We have seen in other shallow-water flows that the imprint of the B component in the unstable eigenmode fades as $\overline{q}$ changes from stepwise uniform to continuously non-uniform. *Dritschel and Vanneste* [2006] also report significant changes in the behavior of the shear wave when $\overline{q}$ is smoothed over the front.

Both the G and B components are close to where $\overline{q}_y = 0$ (indicated by a red straight line in Fig. 2.8, and the $\overline{q}_y$ profile for this mean flow is shown in the bottom of Fig. 2.7), but they are located at different sides of $\overline{q}_y = 0$. For instance in Fig. 2.8, the G component has a negative phase speed without the mean flow and it appears in the $y$ region where $\overline{u}$ is positive, so the magnitude of its phase speed becomes a smaller negative value with the Doppler shift according to (2.13). The B component occurs in the $y$ region where $\overline{q}_y$ is negative which yields a positive phase speed, and the local $\overline{u}$ is negative, so the phase speed becomes a small negative value from the estimation (2.11). This is a consistent explanation for how the B and G modes resonate and lead to an instability. A similar explanation applies to all the B-G instabilities in $j = 1$, 2 and 3.

The four types of mean flow behave differently in ageostrophic instabilities (as shown in Fig. 2.3 to 2.6). In the Bickley jet ($j = 1$), we can only find the B-G instability. This is because the Bickley jet does not have both $\overline{u} > 0$ and $\overline{u} < 0$. The phase speed of the two groups of G modes cannot be shifted in the opposite direction to reach $\hat{C_p}^+ = \hat{C_p}^-$. Though the $j = 2$ flows have both positive and negative $\overline{u}(y)$, the ageostrophic instability is significantly different. For moderate $Ro$ and $Fr$, the cyclonic shear has both a G-G mode and a B-G mode, while we do not find G-G modes in the anticyclonic shear. The G-G instability occurs in $j = 2$ (anticyclonic) only for a $Ro$ value over 10. According to (2.13), with the local $\overline{u}$ having the same magnitude, the phase speed of the G mode depends on the local $\overline{h}$. The cyclonic shear has a negative $\overline{h}$, so it has a smaller phase speed magnitude than the anti-cyclonic shear. Therefore, the G-G instability is more likely to occur in the cyclonic shear than in the anticyclonic shear.

## 2.5 *Ro* and *Fr* Dependence, Degree of Ageostrophy and Energy Diagnostics

### 2.5.1 *Ro* and *Fr* Dependence

For an intermediate $Ro$ and $Fr$, the balanced modes (B-B) and ageostrophic modes (B-G and G-G) coexist in our mean flows, occurring at different spatial scales. As $Ro$, $Fr \to 0$, only the B-B instability occurs. As $Ro$ and $Fr$ increase, the ageostrophic instability begins to appear. In this section we address two questions: 1) In what $Ro$ and $Fr$ regime does the ageostrophic instability begin to appear? 2) As $Ro$ and $Fr$ increase, how does the growth rate of the balanced and ageostrophic instabilities change?

*Ripa* [1983] derived two sufficient stability conditions for a shallow water parallel flow: if there exists any constant value of $\alpha$ such that

$$(\alpha - \overline{u}(y))\frac{d\overline{q}(y)}{dy} \geqslant 0 \tag{2.14}$$

and

$$Fr^2(\alpha - \overline{u}(y))^2 \leqslant 1 + \frac{Fr^2}{Ro}\overline{h}(y) \tag{2.15}$$

for all $y$, then the flow is stable to infinitesimal perturbations. In other words, if for all $\alpha$ one of the conditions is violated at some $y$, the flow may be unstable. The first condition is associated with Rayleigh's inflection-point condition, and is familiar in classical barotropic instability. The second condition refers to a local Froude number $\tilde{Fr}(y)$ defined by:

$$\tilde{Fr}(y) = Fr\frac{|\overline{u}(y)|}{\sqrt{1+\frac{Fr^2}{Ro}\overline{h}(y)}}\ . \tag{2.16}$$

Instability occurs when the local $\tilde{Fr}(y)$ is large enough (not the bulk $Fr$). Note that if taking $\alpha = 0$, (2.15) implies that the flow is stable when $\tilde{Fr} \leqslant 1$. However, because (2.15) is a sufficient condition and $\alpha$ could be any constant value, the real critical $\tilde{Fr}$ for the occurrence of the ageostrophic instability is not exactly 1 (Fig. 2.12). $\tilde{Fr}$ represents the local ratio of the strength of mean flow to that of the inertia-gravity wave speed, taking into account the surface elevation effect. For the occurrence of a G-G mode or a B-G mode, the G mode has to be Doppler shifted by an opposite-signed local $\overline{u}$ (Sec: 2.4). To have an effective Doppler shift, the mean flow velocity should be comparable to the phase speed of a free G mode, which requires a local $\tilde{Fr}$ of order 1.

Figure 2.11 shows the relation between $\tilde{Fr}(y)$ and the eigenmode patterns for the four types of mean flow (One example is shown for each flow). The fluctuation field is concentrated in the $y$ region where the local $\tilde{Fr}(y)$ is larger than a critical value and decays outside that region for all the ageostrophic unstable modes in the mean flows. As shown in Fig. 2.11, for the same $Ro$ (1.0) and bulk $Fr$ (0.7), the local $\tilde{Fr}$ is different in $j = 2$ flows. Due to the surface elevation effect, the cyclonic shear has a larger local $\tilde{Fr}$ than the anticyclonic shear, which implies that the occurrence of an ageostrophic instability requires a larger $Ro$ and bulk $Fr$ in the anticyclonic shear flow (Sec. 2.4). With the assumption $(u', v', h') = Re[\,(\hat{u}(y), \hat{v}(y), \hat{h}(y))e^{i(kx-\omega t)}\,]$ (Sec. 2.1), the fluctuation equations (2.2) can be simplified to a second-order differential equation in $y$: $\frac{d^2\eta}{dy^2} + \chi(y)\frac{d\eta}{dy} + \gamma(y)\eta = 0$, where $\eta$ could be either $\hat{u}$, $\hat{v}$ or $\hat{h}$. Neglecting the $\chi(y)\frac{d\eta}{dy}$ term (which is much smaller than the other two terms in our problem) and considering the behavior of $\eta$ in a local view, the sign of $\gamma(y)$ determines whether the the solution

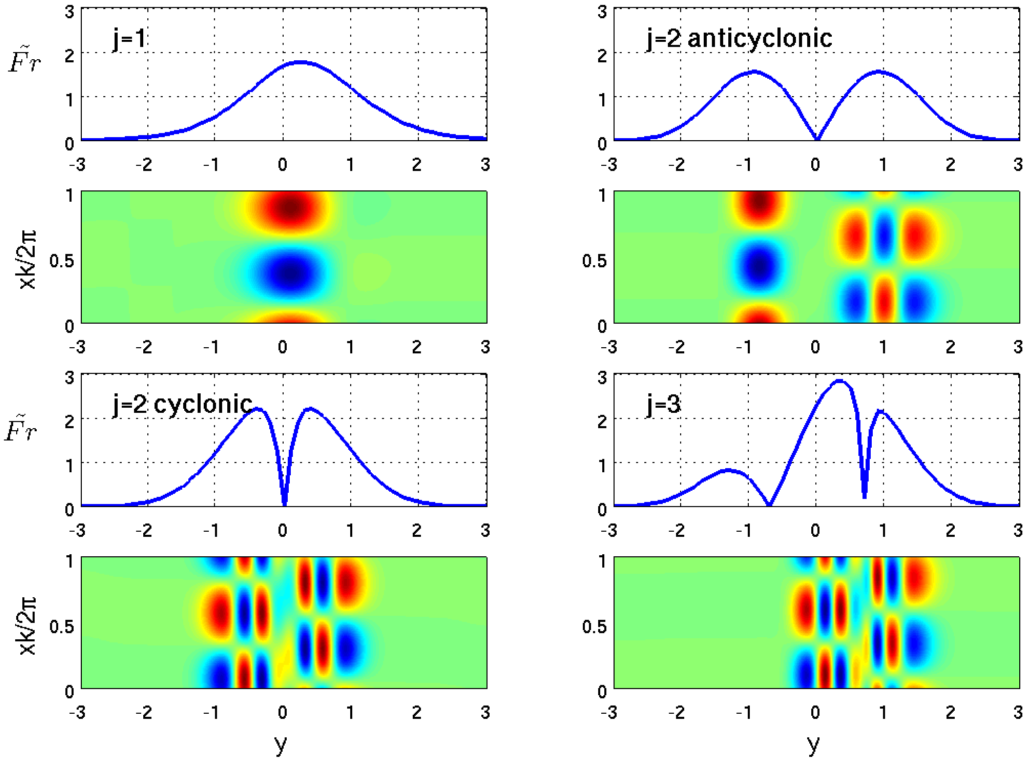

Figure 2.11: The local $\tilde{Fr}(y)$ for the mean flows (upper plots) and the associated $h'$ field (lower plots) for the unstable ageostrophic modes. For $j = 1$, $Ro = 1.0$ and $Fr = 0.50$. For $j = 2$ (anticyclonic), $Ro = 1.0$ and $Fr = 2.50$. For $j = 2$ (cyclonic), $Ro = 1.0$ and $Fr = 0.70$. For $j = 3$, $Ro = 1.0$ and $Fr = 0.99$. A G-G mode is chosen in $j = 2$ and 3, and a B-G mode is chosen in $j = 1$.

oscillates or decays with $y$. $\gamma(y)$ is approximately proportional to $\tilde{Fr}^2(y) - \phi(y)$ (the detailed derivation is not shown). When $\tilde{Fr}(y)$ is above a certain value, $\gamma(y) > 0$, the fluctuation has an oscillatory pattern where the unstable mode amplitude is large; when $\tilde{Fr}(y)$ is smaller than the threshold, $\gamma(y) < 0$, the magnitude of the fluctuation decays and disappears. This relates $\tilde{Fr}(y)$ to the edge of the unstable modes (shown in Fig. 2.11), and indicates that the existence of an unstable ageostrophic mode requires a sufficiently large local $\tilde{Fr}$.

Figure 2.12 shows the maximum growth rate in the ($Ro$, $Fr$) space for the B-B, B-G

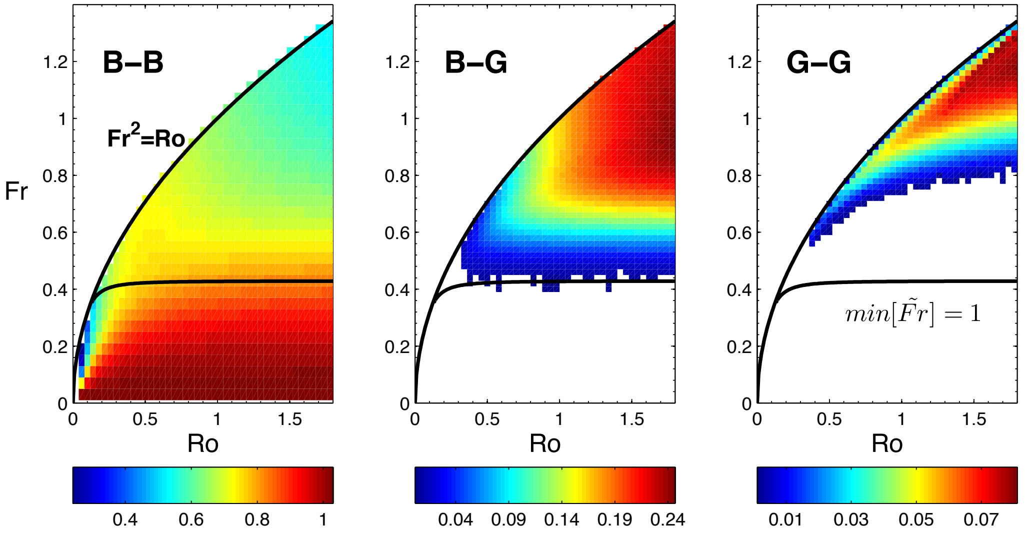

Figure 2.12: The $\sigma$ values in the ($Fr$, $Ro$) space for the three types of unstable modes (B-B, B-G and G-G) in $j = 3$. The upper solid black curve $Fr^2 = Ro$ shows the limits for the existence of a geostrophic mean flow. The lower black line is the contour for $\min[\tilde{F}r(y)] = 1$. For the B-B and B-G modes, we choose the maximum growth rate for each $Ro$ and $Fr$. For the G-G mode, we choose the maximum growth rate of a particular mode $P_{1.5}$-$N_1$. We have checked and confirmed that other G-G modes behave the same as this one for the dependence of $Ro$ and $Fr$.

modes and a particular G-G mode ($P_{1.5}$-$N_1$), in $j = 3$. For B-B instability, the growth rate almost does not depend on $Ro$ at a small $Fr$ (<0.1), consistent with the classical barotropic instability of a 2D fluid. For $Fr < 0.4$, the growth rate increases with increasing $Ro$, while for $Fr > 0.4$ the growth rate decreases slightly with increasing $Ro$. For a fixed $Ro$, the growth rate of B-B instability weakens significantly with increasing $Fr$, especially for the small $Ro$. On the contrary, the ageostrophic instabilities (B-G and G-G) are more unstable for a larger $Fr$. The strongest growth rate of the ageostrophic instability appears just below the edge for the existence limit of a geostrophic mean flow (indicated by the upper black line; Sec. 2.1). The B-G instability is stronger than the G-G instability, and starts to appear at a lower $Fr$ value than the G-G instability. The line $\min[\tilde{Fr}(y)] = 1$ is plotted by the lower black curve. The two black lines roughly enclose the regime for the B-G instability. Although not shown in Fig. 2.12 (right), the line $\min[\tilde{Fr}(y)] = 1.7$ roughly marks the lower limit of the G-G instability. This confirms that the ageostrophic instabilities are associated with the violation of Ripa's second condition. For intermediate $Ro$ and $Fr$ (order 1) in $j = 3$, the growth rate of ageostrophic modes is small compared with the balanced mode. However, with increasing $Ro$ and $Fr$, the growth rate of the balanced instability decreases, while that of the ageostrophic instability increases. At a large $Ro$ and $Fr$, the ageostrophic instability would be stronger than the balanced one. The relative strength of the three instabilities varies significantly among different types of flow. For instance, in $j = 2$ (cyclonic), the B-G ageostrophic instability is the most unstable one among the three instabilities for $Ro = 1.0$ and $Fr = 0.70$ (Fig.2.4), i.e., the ageostrophic instability is dominant over the balanced one. In contrast, the balanced instability is the dominant one in $j = 2$ (anticyclonic) and Bickley jet for $Ro = 1.0$.

### 2.5.2 Degree of Ageostrophy

Besides the difference in the growth rate dependence on $Fr$, the balanced instability and ageostrophic instability have significant difference in the degree of ageostrophy for the eigenmodes. We use the divergent component of the fluctuation velocity to represent the degree of ageostrophy, which is defined as

$$\delta = \frac{\left\|\vec{u}'_{div}\right\|}{\left\|\vec{u}'\right\|} = \sqrt{\frac{\int (\overline{u'^2_{div}} + \overline{v'^2_{div}})dy}{\int (\overline{u'^2} + \overline{v'^2})dy}} \,. \tag{2.17}$$

The divergent velocity is evaluated by $\vec{u}'_{div} = \vec{u}' - \vec{u}'_{geo}$, where $\vec{u}'_{geo} = \hat{z} \times \nabla\psi'$. The vorticity of the fluctuation is the same as the geostrophic component: $\zeta' = \hat{z} \cdot (\nabla \times \vec{u}') = \hat{z} \cdot (\nabla \times \vec{u}'_{geo}) = \nabla_h^2 \psi'$, and we obtain $\psi'$ by $\psi' = \nabla_h^{-2} \zeta'$. $\delta$ for the three instabilities versus $Fr$ is plotted for a fixed $Ro = 1.0$ in Fig. 2.13. The B-B eigenmode has a zero divergent component at small $Fr$. Though the divergent part increases with $Fr$, it remains small for a broad range of finite $Fr$. With a finite $Ro$ and $Fr$ effect, the mode is still balanced (Sec 2.2.1 and 2.3). For B-G and G-G modes, the divergent velocity is dominant, indicating that the fluctuation is highly ageostrophic. When the ageostrophic instability starts to appear at the critical $Fr$ (roughly 0.4 for B-G and 0.7 for G-G), the growth rate is weak and the mode is mostly a neutral G mode that is not coupled with the mean shear, so the fluctuation is almost purely divergent ($\delta \sim 1$). When $Fr$ increases, the mean flow interacts with the G mode, leading to unstable modes. The unstable mode is not purely divergent due to the participation of the mean flow. The B-G mode involves the interaction between a B mode and a G mode, so the ageostrophic degree is smaller than a G-G mode. Though the result is shown for a fixed $Ro = 1.0$, the conclusion discussed above remains the same for different $Ro$ cases. The higher-order balance for the instabilities is not checked in our work. However, because both the B-G and G-G instabilities clearly involve a coupling with inertia-gravity waves, they are unbalanced instabilities.

### 2.5.3 Energy Diagnostics

To reach a more complete view of the unstable modes, the energetics is examined. In the linearized shallow water system, we express the total energy $E$ as the sum of the

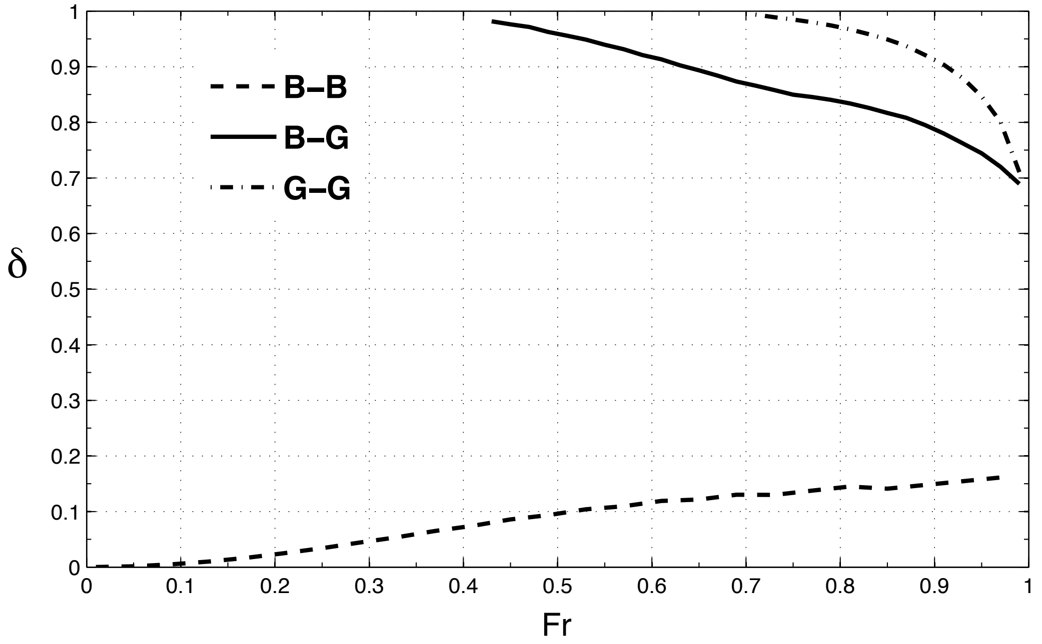

Figure 2.13: The ratio of the divergent component in fluctuation velocity $\delta = \frac{\|\vec{u}'_{div}\|}{\|\vec{u}'\|}$ for the B-B, B–G and G-G modes in $j = 3$, for a fixed $Ro = 1.0$. The same unstable modes as in Fig.2.12 are chosen to calculate this ratio.

mean energy $\overline{E}$ and the quadratic fluctuation energy $E'$:

$$\overline{E} = \int [\,\frac{1}{2}(1+\frac{Fr^2}{Ro}\overline{h})\overline{u}^2 + \frac{1}{2}\frac{Fr^2}{Ro^2}\overline{h}^2 + \frac{1}{Ro}\overline{h}\,]dy \tag{2.18}$$

$$E' = \int [\,\frac{1}{2}(1+\frac{Fr^2}{Ro}\overline{h})(\overline{u'^2}+\overline{v'^2}) + \frac{1}{2}\frac{Fr^2}{Ro^2}\overline{h'^2} + \frac{Fr^2}{Ro}\overline{u}\,\overline{h'u'}\,]dy\ , \tag{2.19}$$

where the overhead bar means zonal average. The total energy $E = \overline{E} + E'$ is conserved without viscosity. The energy balance for the mean flow and the fluctuations are

$$\begin{aligned} \frac{dE'}{dt} &= \int [\,(1+\frac{Fr^2}{Ro}\overline{h})\overline{u}\,\overline{v'\frac{\partial u'}{\partial y}} - \frac{Fr^2}{Ro^2}\overline{h'v'}(Ro\overline{u}\frac{\partial \overline{u}}{\partial y} + \frac{\partial \overline{h}}{\partial y})\,]dy \\ \frac{d\overline{E}}{dt} &= \int [-(1+\frac{Fr^2}{Ro}\overline{h})\overline{u}\,\overline{v'\frac{\partial u'}{\partial y}} + \frac{Fr^2}{Ro^2}\overline{h'v'}(Ro\overline{u}\frac{\partial \overline{u}}{\partial y} + \frac{\partial \overline{h}}{\partial y})\,]dy\ . \end{aligned} \tag{2.20}$$

The first conversion term is related to the horizontal Reynolds stress (as in classical barotropic instability), and the second is related to eddy mass flux (Stokes drift).

The ratio of potential to kinetic energy of the fluctuations $PE/KE$ is examined, where $PE = \int \frac{1}{2}\frac{Fr^2}{Ro^2}\overline{h'^2}$ and $KE = \int \frac{1}{2}(1+\frac{Fr^2}{Ro}\overline{h})(\overline{u'^2}+\overline{v'^2})$. $KE$ is dominant for all three types of instability. The $PE/KE$ ratio is larger in the ageostrophic instabilities than in the balanced instability. For the conversion between $\overline{E}$ and $E'$, the first and second terms in (2.20) have the same sign in the balanced instability, but have opposite signs in the ageostrophic ones, implying that the ageostrophic unstable fluctuations transfer energy to the mean flow through the mass fluxes. The first conversion term, horizontal Reynolds stress, is dominant for all three types of instability.

## 2.6 A Nonlinear Example of Ageostrophic Instability: Modon

In $j = 2$ (cyclonic), the ageostrophic instability is dominant over the balanced one for intermediate $Ro$ and $Fr$ values. Compared with the cyclonic case, the balanced instability is stronger, and the ageostrophic instability is weaker for $j = 2$ (anticyclonic), with the same $Ro$ and $Fr$. This asymmetry is also seen in $j = 3$, where the balanced instability appears in the region with negative potential vorticity, and the ageostrophic instability appears in the region with positive potential vorticity and large local $\tilde{Fr}$.

Therefore, in the nonlinear time evolution of a rotating shallow water flow for a finite $Ro$ and $Fr$, it is expected that the ageostrophic instability would appear in a cyclone. This expectation is borne out in the time evolution of a modon for finite $Ro$.

A modon, as well studied by *McWilliams* [1981] and *Kizner et al.* [2008], is a steadily propagating dipole. The steady modon solution for $Ro = 0.2$ and $Fr = 0.2$ in *Kizner et al.* [2008] is taken as the initial condition for the time-integration study of nonlinear shallow water equations (2.1). The surface elevation $h$, potential vorticity $q$, and local $\tilde{Fr}$ of the modon solution are shown in the first row of Fig. 2.14, where

$$q = \frac{1 + Ro(v_x - u_y)}{1 + \frac{Fr^2}{Ro}h}, \qquad \tilde{Fr} = Fr\frac{|\vec{u}|}{\sqrt{1 + \frac{Fr^2}{Ro}h}}.$$

Note that here $u$, $v$, $h$ and $q$ are non-dimensional variables. The $y$ profiles at $x = 0$ are shown in the second row. In order for the modon to steadily propagate, the strength of the cyclone and that of the anticyclone are quite asymmetric in $h$ and $q$ for finite $Ro$. The extremes of the cyclone are stronger than those of the anticyclone. Unlike the symmetric parallel flows studied in previous sections, the asymmetric modon profile leads to a sizable local $\tilde{Fr}$, even with relatively small bulk $Ro$ and $Fr$.

The time evolution of the ageostrophic instability is shown in the third row in Fig. 2.14. The black thick lines circle the region where $\tilde{Fr}$ is larger than 1 in Fig. 2.14 (the third plot of the first row; the third row). Following with the moving frame of the modon, the plots are zoomed in the cyclone region, which is indicated by the white rectangle in the plots of the first row. The ageostrophic unstable waves are trapped in the cyclone region; as they evolve, they change the shape of the modon, evidently to make it less unstable, and then die away through viscosity. As circled by the thick black lines, the instability appears where the local $\tilde{Fr}$ is large, which is consistent with Ripa's second condition. The evolution of initial modons with smaller $Ro$ and local $\tilde{Fr}$ does not manifest this spontaneous instability.

A linear instability analysis of a modon cross-section profile confirms the above nonlinear result. We take the $y$ profile of $h$ at $x = 0$ as the mean background $\overline{h}$, and

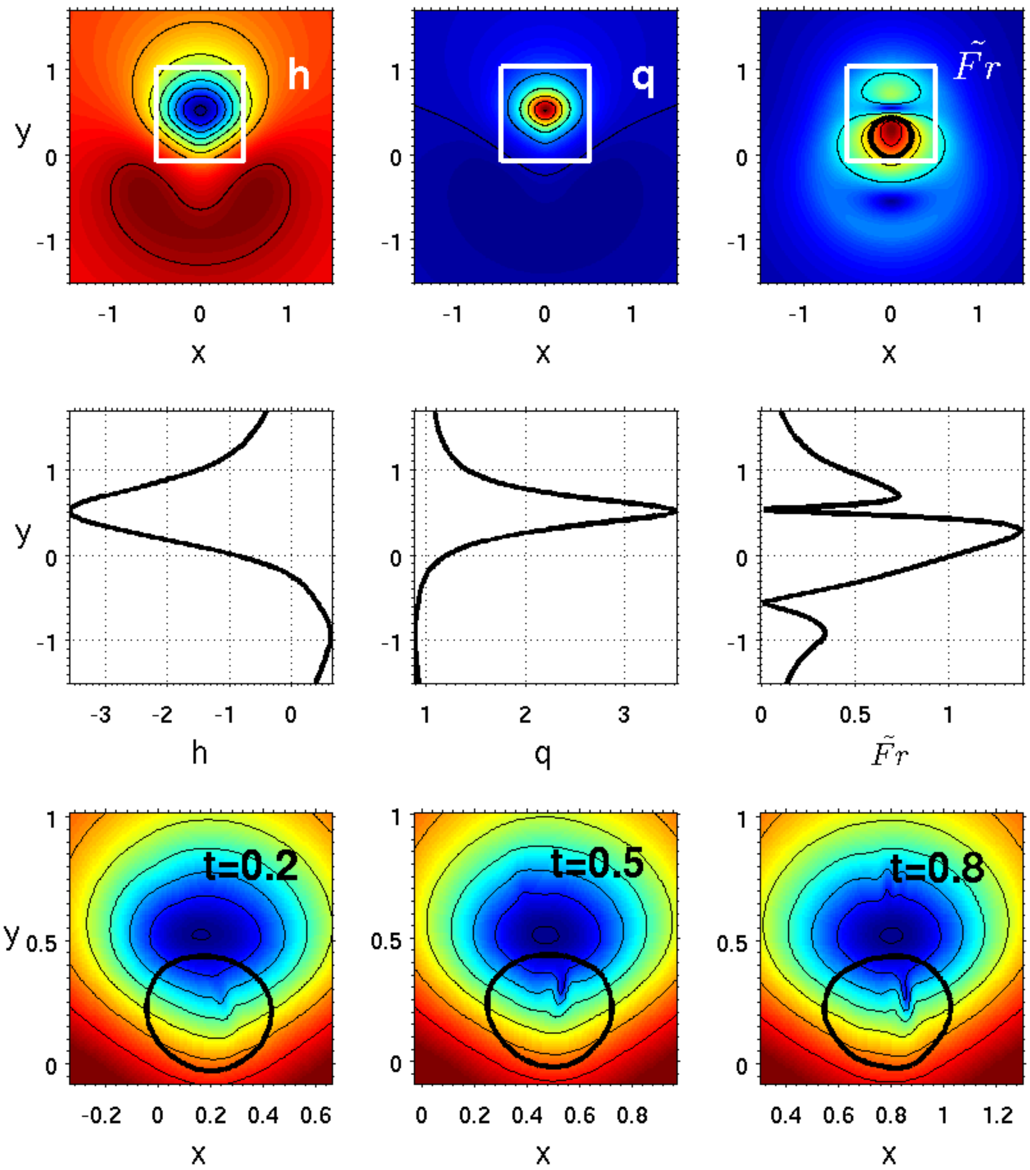

Figure 2.14: The modon initial condition (first two rows) and time evolution (the third row) for $Ro = 0.2$ and $Fr = 0.2$ in the non-dimensional, nonlinear rotating shallow water equations. (To be continued on next page.)

Figure 2.14: (Continue to previous page.) The first row shows the patterns for $h$, $q$, and $\tilde{Fr}$ at $t = 0$. For $h$ contours, the interval is 0.5 and the minimum value is -3.5 (zero contour is not shown). For $q$ contours, the interval is 0.5 and the minimum value is 0.5. For $\tilde{Fr}$ contours, the interval is 0.4 and the minimum value is 0.4. The second row shows $h(y)$, $q(y)$, and $\tilde{Fr}(y)$ at $x = 0$ and $t = 0$. The third row shows the patterns for $h$ at $t = 0.2$, 0.5, and 0.8, respectively. The plot is zoomed-in the region indicated by the white rectangle in the first row, following with the moving-modon. The contours have the same values as in the $h$ plot at $t = 0$. The thick black line circles where $\tilde{Fr} > 1$, both in the $\tilde{Fr}$ plot in the first row and the $h$ plots in the third row.

calculate the $\overline{u}$ that is in geostrophic balance with $\overline{h}$. Note that $\overline{u}$ is different from the $y$ profile of $u$ at $x = 0$ of the modon. The $\overline{h}$ and $\overline{u}$ profiles are shown in the upper left column in Fig. 2.15. To be consistent with the nonlinear simulation, we take $Ro = 0.2$ and $Fr = 0.2$ in the linear calculation. We find multiple ageostrophic unstable modes in a range of intermediate and large $k$. The growth rate is significantly large compared to the symmetric idealized flows in early sections (the bottom plot, Fig. 2.15). The $k$ range (5$\sim$10) shown in the plot is consistent with the zonal length scale of the trapped ageostrophic instability occuring in the nonlinear evolution (the third row, Fig. 2.14). The local $\tilde{Fr}(y)$ of the mean flow and an example of the unstable eigenmodes are shown in the upper right column in Fig. 2.15. The ageostrophic mode is trapped in the region where $\tilde{Fr}$ is the largest in $y$, which is consistent with the meridional position of its occurrence in the nonlinear evolution.

This modon example illustrates the transient, nonlinear behavior of an ageostrophic instability in a more complex (nonparallel) flow. The time evolution of a finite $Ro$ modon is also examined by *Ribstein et al.* [2010], where the ageostrophic instability is not observed perhaps due to a lower resolution compared to our simulation. *Lahaye and Zeitlin* [2012] study the time evolution of a geostrophic modon in a higher $Ro$ (0.3 or 0.4) shallow-water model, and find shock formation during the adjustment process. We

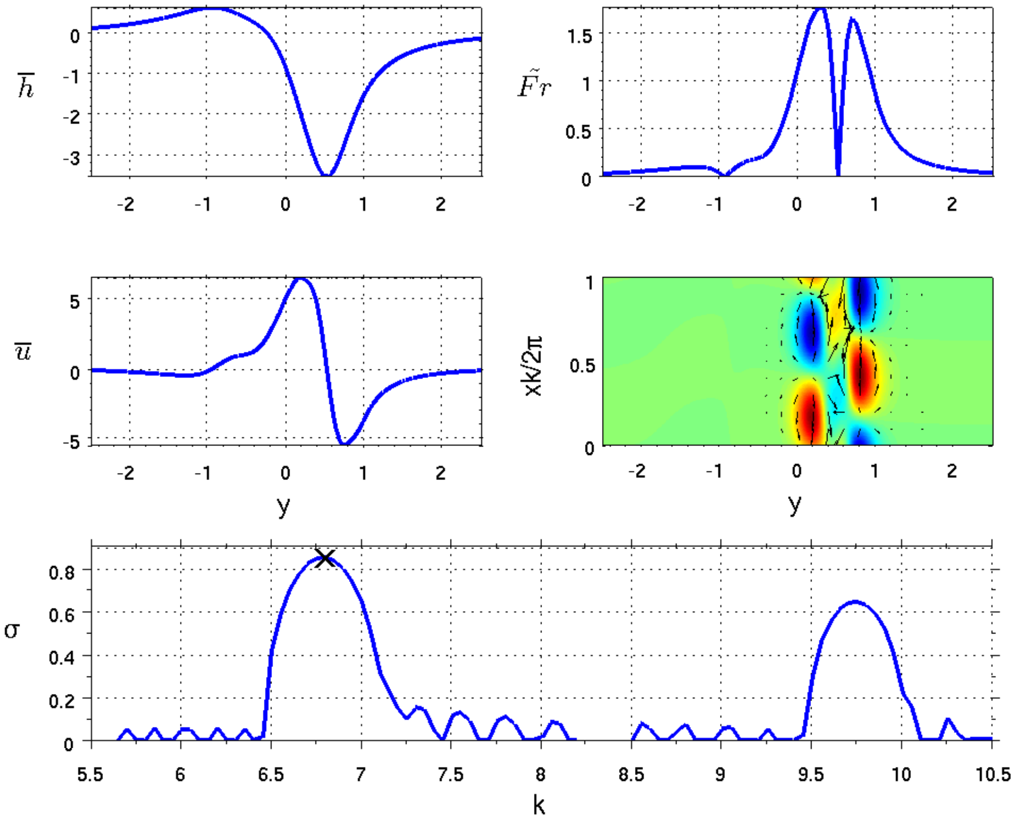

Figure 2.15: The linear instability analysis of the modon cross-section profile for $Ro = 0.2$ and $Fr = 0.2$. The upper left column shows the mean profile $\overline{h}(y)$ and $\overline{u}(y)$. $\overline{h}$ is the cross-section of the steady modon profile at $x = 0$, and $\overline{u}$ is the zonal velocity in geostrophic balance with $\overline{h}$. The bottom plot is the growth rate $\sigma$ versus $k$ for multiple unstable ageostrophic modes. The selected $k$ range is consistent with the length scale of the trapped instability appearing in the nonlinear evolution. The upper right column shows the local $\tilde{Fr}(y)$ and the fluctuation fields of an unstable ageostrophic mode for $k = 6.80$ (marked by a cross in the bottom $\sigma$ plot). $h'$ is shown by the color; $u'$ and $v'$ are shown by the black vector arrows.

do not see similar phenomena in our simulation, perhaps because our initial condition is a steady modon solution to the finite $Ro$ model and hence there is little adjustment. Furthermore, the $Ro$ in our case ($= 0.2$) might be too small for the occurrence of a shock.

## 2.7 Main Conclusions

To identify a general route for the breakdown of balance and the energy transfer towards small scales, the ageostrophic instability of a horizontal interior shear flow is studied in this chapter. We solve for the instabilities in several balanced parallel shear flows $\overline{u}(y)$ (Bickley jet, cyclonic and anticyclonic double jet, and triple jet), with continuous, non-uniform potential vorticity, without side boundaries or vanishing layer depth, in a single-layer $f$-plane rotating shallow water model. In the system, there are mainly two types of neutral modes: B mode and G mode. A neutral B mode is a balanced shear wave mode that exists due to the potential vorticity gradient. A neutral G mode is an inertia-gravity wave mode. The resonant coupling of two neutral modes yields three types of instability: B-B, B-G and G-G. B-B instability is the balanced shear instability (classical barotropic instability) that relates to Rayleigh's inflection point condition. Both B-G and G-G are unbalanced instabilities, which are highly ageostrophic and occur when the local $\tilde{Fr}$ is sufficiently large (associated with Ripa's second stability condition). The resonant G component can be clearly identified in the ageostrophic instabilities. However, the B-G instability involves a set of B modes due to a continuously varying potential vorticity gradient, so its resonant B component is less evident in the unstable modes. The balanced instability is suppressed by large $Fr$, while the growth rate of the ageostrophic instability increases with increasing $Fr$. For moderate $Ro$ and $Fr$, all three types of instability appear in the cyclonic double jet and the triple jet, but only B-B and B-G instabilities appear in the anticyclonic double jet and the Bickley jet. The G-G instability can be found in the anticyclonic double jet for large $Ro$ and $Fr$ but never appears in the Bickley jet. In the cyclonic double jet, the ageostrophic instability is dominant over the balanced one for intermediate $Ro$ and $Fr$ values. The ageostrophic instability is manifested in the nonlinear time evolution of a finite $Ro$ modon, appearing in the cyclone region, where the local $\tilde{Fr}$ is large.

As proposed in *McWilliams et al.* [1998], three criteria are related to the breakdown of balance in a 3D flow, and they are associated with three types of instabilities. The $N^2$ (gravitational instability) and $A$ (centrifugal instability) conditions do not apply to the single-layer shallow water model. They both involve vertical overturning in the unstable eigenmodes. The $A - S$ condition for the mean flow in the shallow water system is

$$\overline{A} - \overline{S} = 1 - Ro\overline{u}_y - Ro\left|\overline{u}_y\right| . \tag{2.21}$$

We check the critical $Ro$ where $\min(\overline{A} - \overline{S})$ changes sign and find that it greatly precedes the onset of ageostrophic instabilities, hence is not evidently relevant to shallow-water instabilities, perhaps for the same reason of the lack of overturning modes. In contrast, Ripa's second stability condition is more relevant to the instability cases in the shallow water model. This suggests that the processes leading to loss of balance can be rather different in 3D and shallow water fluids.

# CHAPTER 3

# Ageostrophic Instability in Rotating, Stratified Vertical Shear Flows

In this chapter we focus on the linear instabilities of a rotating, stably stratified (constant $N^2$), interior baroclinic shear flow $\overline{U}(z)$ with non-uniform potential vorticity in Boussinesq equations. The chapter is constructed as follows: Section 3.1 specifies the equations, the non-dimensional parameters, and the mean flows. The first type of ageostrophic instability (AI1), a transformation between BCI and CI, is decribed in Sec. 3.2, followed by Sec. 3.3 for the second type of ageostrophic instability (AI2) that is associated with inertial critical layers. Sec. 3.4 briefly summarizes the main conclusions.

## 3.1 Equations, Paramters and Mean Flows

We solve the instability problem with a f-plane, constant-stratification ($N^2$ = constant), linearized Boussinesq equations. To non-dimensionalize the variables, we scale them as follows:

$$(x,y) \to L\,,\;\; z \to H\,,\;\; (u,v) \to U_0\,,\;\; w \to W_0 = \frac{fU_0^2}{N^2H}\,,\;\; p \to fU_0\rho_0 L\,,\;\; b \to \frac{fU_0L}{H}\,,$$

where $f$ and $N$ are Coriolis and buoyancy frequencies, $\rho_0$ is the average density. For a small perturbation around the mean state $\overline{U}(z)$, $\overline{B}(y,z)$, and $\overline{P}(y,z)$ the linearized non-dimensional Boussinesq equations are

$$\begin{cases} Ro(\frac{\partial u'}{\partial t} + \overline{U}\frac{\partial u'}{\partial x} + \frac{Ro}{Bu}\overline{U}_z w') - v' + \frac{\partial p'}{\partial x} & = & 0 \\ Ro(\frac{\partial v'}{\partial t} + \overline{U}\frac{\partial v'}{\partial x}) + u' + \frac{\partial p'}{\partial y} & = & 0 \\ \lambda^2 \frac{Ro^2}{Bu}(\frac{\partial w'}{\partial t} + \overline{U}\frac{\partial w'}{\partial x}) - b' + \frac{\partial p'}{\partial z} & = & 0 \\ \frac{\partial u'}{\partial x} + \frac{\partial v'}{\partial y} + \frac{Ro}{Bu}\frac{\partial w'}{\partial z} & = & 0 \\ \frac{\partial b'}{\partial t} + \overline{U}\frac{\partial b'}{\partial x} + \overline{B}_y v' + \frac{Ro}{Bu}\overline{B}_z w' & = & 0\,. \end{cases} \tag{3.1}$$

There are three important non-dimensional parameters in the equations: Rossby number $Ro$, Burger number $Bu$, and aspect ratio $\lambda$,

$$Ro = \frac{U_0}{fL}, \quad Bu = \left(\frac{NH}{fL}\right)^2, \quad \lambda = \frac{H}{L}\,.$$

The Froude number can be defined by $Ro$ and $Bu$: $Fr = \frac{U_0}{NH} = \frac{Ro}{\sqrt{Bu}}$. Because the mean flow velocity $\overline{U}(z)$ is uniform in the horizontal plane, the horizontal length scale $L$ is arbitrary. Therefore, the three parameters ($Ro$, $Bu$, $\lambda$) are not independent of each other. We choose $Bu = 1$ (a typical value for mesoscale eddies or synoptic storms), and then $Ro$ and $\lambda$ become free parameters. For the large-scale or mesoscale (synoptic-scale) flows, the horizontal scale is much larger than the vertical scale, so we choose a small value of aspect ratio ($\lambda = 0.01$ in our study). We look for the ageostrophic instability in a balanced flow for intermediate $Ro$. The mean flow satisfies thermal-wind balance $\overline{B}_y = -\overline{U}_z$, so

$$\vec{V}(z) = (\overline{U}(z),\ 0,\ 0)\,, \quad \overline{B}(y,z) = \frac{Bu}{Ro}z - \overline{U}_z y\,.$$

Here the first term in $\overline{B}$ is caused by the background stratification, and the second term represents the horizontal buoyancy slope induced by the thermal-wind balanced vertical shear. The vertical gradient of buoyancy is $\overline{B}_z = \frac{Bu}{Ro} - \overline{U}_{zz}y$. If $Ro$ and the meridional scale of the fluctuation are not large, the first term is dominant over the second. We consider solutions with small and intermediate $Ro$ or meridional scale, so the second term in $\overline{B}_z$, $-\overline{U}_{zz}y$, is dropped in the buoyancy equation by solving the problem in the neighborhood of $y = 0$. This allows a solution with an $\mathrm{e}^{ily}$ form in the meridional direction. Then, the above assumption is valid when $Ro$ is not large or $l$ is not small. With this simplification, we can assume $(u', v', w', p', b') \sim \mathrm{Re}[(\hat{u}, \hat{v}, \hat{w}, \hat{p}, \hat{b})e^{i(kx+ly)}e^{\sigma t}]$ (the real part of $\sigma$ is the growth rate, and we use $\omega = -\mathrm{Imag}(\sigma)$ to denote frequency), and then (3.1) becomes a 1D eigenvalue problem in $z$:

$$\begin{cases} Ro(\sigma\hat{u} + ik\overline{U}\hat{u} + Ro\overline{U}_z\hat{w}) - \hat{v} + ik\hat{p} &= 0 \\ Ro(\sigma\hat{v} + ik\overline{U}\hat{v}) + \hat{u} + il\hat{p} &= 0 \\ \lambda^2 Ro^2(\sigma\hat{w} + ik\overline{U}\hat{w}) - \hat{b} + \dfrac{\partial\hat{p}}{\partial z} &= 0 \\ ik\hat{u} + il\hat{v} + Ro\dfrac{\partial\hat{w}}{\partial z} &= 0 \\ \sigma\hat{b} + ik\overline{U}\hat{b} - \overline{U}_z\hat{v} + \hat{w} &= 0\,. \end{cases} \tag{3.2}$$

We solve this system for small $\lambda = 0.01$ and $Ro$ increasing from 0 to values beyond the onset condition for CI, but below that for KHI. The problem is solved by a Fortran code with ARPACK library (an eigensolver library). Because a large resolution is needed for an accurate solution, it is too expensive to compute the full-spectrum of eigenvalues. ARPACK computes a few eigenvalues and corresponding eigenfunctions close to the given "target" (guessed eigenvalue) by a iterative convergence process. The differential operators are discretized by a second-order centered finite-difference method, in a staggered grid, with a resolution of $N \sim 5000$ in the vertical direction. For the interior vertical shear flows, the domain in the computation is sufficiently large to remove the boundary influence on the unstable modes. We choose a rigid boundary condition $w' = 0$ and $\frac{\partial u'}{\partial z} = \frac{\partial v'}{\partial z} = \frac{\partial p'}{\partial z} = \frac{\partial b'}{\partial z} = 0$. We do not look for radiating instabilities by setting a propagating boundary condition, therefore none of the unstable modes found by our eigensolver has a vertical propagation. We increase the grid resolution from 3000 to 10000, and have confirmed with that the eigenvalue converges well with $N = 5000$ for the unstable modes of interest.

Two types of interior vertical shear flows are examined: the hyperbolic tangent flow (TANH) and the double-jet flow (DJET). Although the EADY flow has been well

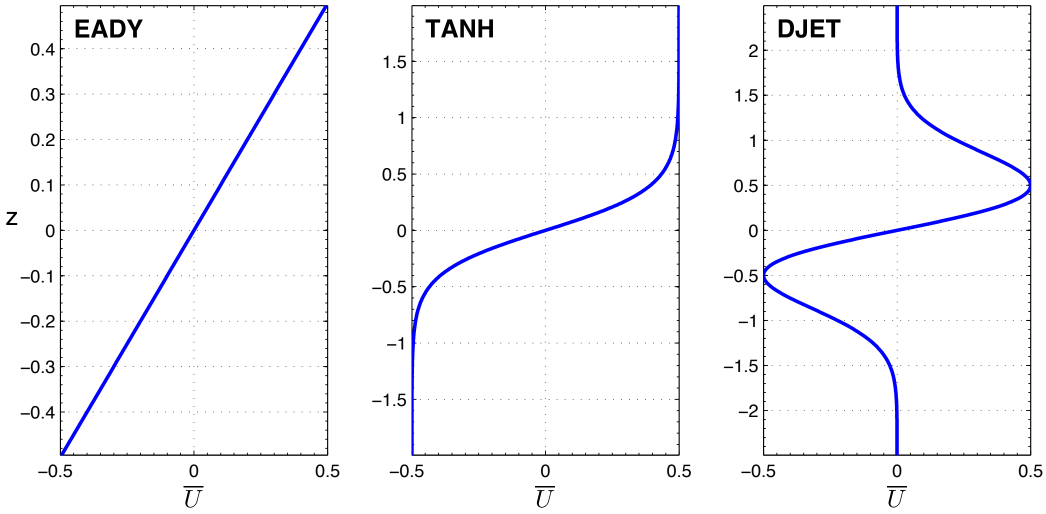

Figure 3.1: The mean flow velocity profiles $\overline{U}(z)$ for the EADY flow, hyperbolic tangent (TANH) flow, and the double-jet (DJET) flow. All the velocity profiles have the same maximum magnitude (0.5), and the velocity difference between [-0.5, 0.5] is about 1. For EADY the vertical boundaries are at $|z| = 0.5$, and for the others they are at much longer $|z|$.

studied by earlier literature, we reproduce some instability results of it for comparison with the TANH and DJET flows. The analytical forms for the mean flows $\overline{U}(z)$ are

$$\text{EADY}: \overline{U} = z, \ \text{TANH}: \overline{U} = 0.5\times\tanh(2.65z), \ \text{and DJET}: \overline{U} = \mathrm{e}^{0.5} z \mathrm{e}^{-2z^2}, \text{ respectively.}$$

The velocity profiles of the mean flows are shown in Fig. 3.1. The velocities are normalized to have the same maximum magnitude $\left|\overline{U}(z)\right|_{\text{max}} = 0.5$, and the vertical distance between $\overline{U}_{\text{max}}$ and $\overline{U}_{\text{min}}$ is 1 for EADY and DJET flows, and about 1 for the TANH flow. All of these $\overline{U}(z)$ are odd-symmetric about $z = 0$. Because the TANH flow is simpler than the DJET flow and thus easier to understand, our main results and discussion in the next two sections will focus on this flow.

We now consider the *Ro* regimes for instabilities discussed in Sec. 1.2. At $Ro \to 0$, the classic baroclinic instability occurs if inflection points exist (as they do here). As *Ro* increases, the conditions are satisfied in the following order: 1) $A - S = 0$ is satisfied,

Table 3.1: Critical $Ro$ for the occurrence of anticyclonic, ageostrophic instability (AAI), centrifugal instability (CI), and Kelvin-Helmholtz instability (KHI) in the three mean flows.

| Flow | AAI | CI | KHI |
|---|---|---|---|
| EADY | 0.71 | 1 | 2 |
| TANH | 0.53 | 0.75 | 1.51 |
| DJET | 0.43 | 0.61 | 1.21 |

and anticyclonic, ageostrophic instability (AAI) occurs or has a significant growth rate beyond this $Ro$; 2) $A = 0$ is satisfied, and the centrifugal instability (CI) begins to occur; 3) the onset condition for the classic Kelvin-Helmholtz instability (KHI) (non-rotating) $Ri < \frac{1}{4}$ is reached; 4) if $N^2 < 0$, the gravitational instability would occur. The $Ro$ criteria for the occurrence of AAI, CI, and KHI in the three types of mean flow are calculated and listed in Table 3.1. The criteria are calculated by evaluating the $Ro$ values that satisfy $\min(\overline{A}\text{-}\overline{S}) = 0$, $\min(\overline{A}) = 0$, and $\min(Ri) = \frac{1}{4}$, respectively. For an interior vertical shear $\overline{U}(z)$,

$$\overline{A} = 1 - Ro^2\overline{U}_z^2\,, \quad \overline{S} = Ro^2\overline{U}_z^2\,, \quad \text{and} \quad \overline{Ri} = 1/Ro^2\overline{U}_z^2\,,$$

where $A$ and $S$ are non-dimensionalized by $f$. The non-dimensional $PV_{Ertel}$, scaled by $fN^2$, is

$$\overline{PV}_{Ertel} = 1 - Ro^2\overline{U}_z^2\,.$$

Note that for both $\overline{A}$ and $\overline{PV}_{Ertel}$, we have dropped the term $-Ro\overline{U}_{zz}y$ with the assumption that we solve the problem for non-large $Ro$ or non-small $l$ in the neighborhood of $y = 0$.

## 3.2 AI1: A Continuous Transformation Between BCI and CI

For the three types of $\overline{U}(z)$ with a zero vertical average (Fig. 3.1), the dominant BCI in the quasigeostrophic regime has a vertically symmetric mode structure (The eigenvalue

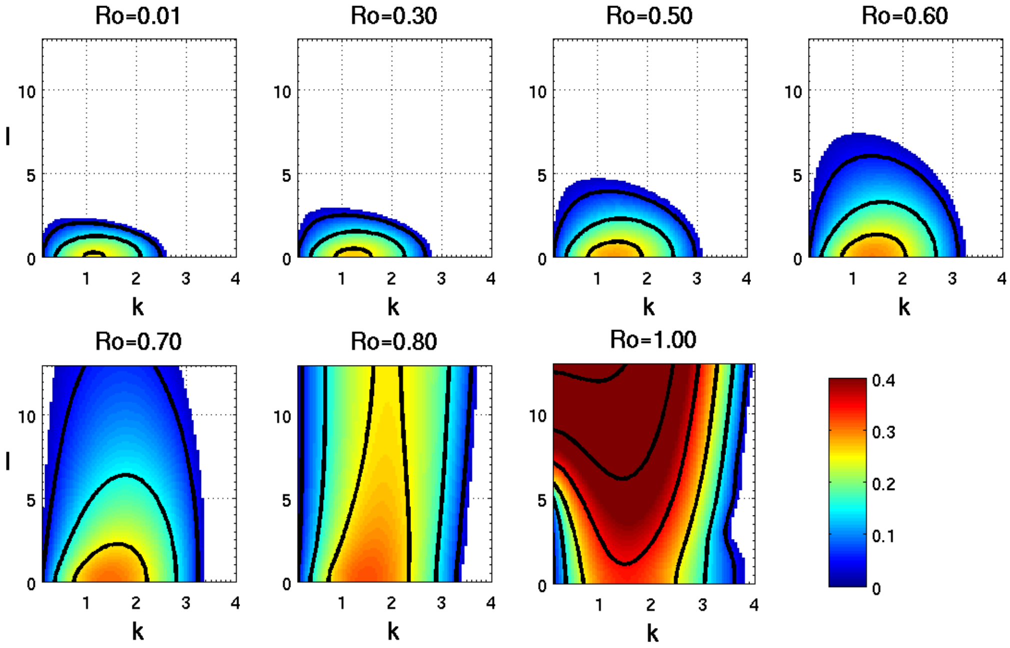

Figure 3.2: The growth rate of the vertically symmetric mode ($\omega = 0$) in the TANH flow in a ($k$, $l$) space with increasing $Ro$. The minimum value for the contours is 0.05, and their interval is 0.1.

$\sigma$ of this mode only has a real part ($\omega = 0$), and the eigenfunction satisfies [$\hat{u}(z)$, $\hat{v}(z)$, $\hat{w}(z)$, $\hat{p}(z)$, $\hat{b}(z)$] = [$i\hat{u}^*(-z)$, $i\hat{v}^*(-z)$, $i\hat{w}^*(-z)$, $-i\hat{p}^*(-z)$, $i\hat{b}^*(-z)$], where $^*$ denotes complex conjugate), with zero frequency. As *Ro* increases, this BCI mode becomes less unstable, and its occurrence shrinks to smaller $k$ in the EADY flow, while it becomes more unstable and extends to larger $k$ in the TANH and DJET flows. On the other hand, with increasing *Ro*, this vertically symmetric mode extends to larger $l$ and continuously changes its property in all three mean flows. To be representative of the continuous transformation, the growth rate of the vertically symmetric mode ($\omega = 0$) in the TANH flow in a ($k$, $l$) space, with increasing *Ro* is shown in Fig. 3.2. The vertically symmetric mode is a single mode with continuous transformation, rather than multiple coexisting modes with the same frequency $\omega = 0$. This result is confirmed by a full-spectrum eigenvalue solver with a lower resolution. As *Ro* increases, the mode becomes stronger near $l = 0$ and broadens to larger $k$ and $l$. During the extension to larger $l$, the mode changes and is no longer a BCI mode. At *Ro* = 0.7, this mode has extended to very large $l$ (> 12) and becomes highly ageostrophic at intermediate and large $l$. At *Ro* = 0.8, the CI mode begins to appear at $k = 0$ and large $l$ (the strongest CI mode appears near $l \sim 25$ and hence is not shown in the figure). At *Ro* = 1, the CI mode becomes quite robust near $k = 0$ and $l = 10$; all the unstable modes join together, occuring over small and intermediate $k$, and a wide range of $l$. The behavior of the vertically symmetric modes in the EADY and DJET flows is similar to that in the TANH flow, except that in the EADY flow, all the modes appear in a narrower band of small $k$, especially when $l$ is large. In the continuous transformation with increasing *Ro*, the mode that appears far from $l = 0$ and $k = 0$ is a new type of ageostrophic instability; we name it AI1. It occurs at finite *Ro*, but below the onset *Ro* for CI, and its growth rate increases with increasing *Ro*. There is no clear separation in ($k$,$l$) between either BCI and AI1, or AI1 and CI at any *Ro*, but the characteristics of the three types of instability are distinguishable for an intermediate *Ro* (Fig. 3.3 to 3.5).

The main differences among these three types of unstable modes are manifested by the *Ro* regime for the occurrence of the mode, patterns of the eigenmode, the diagnostics of balance, and the energetics. For the diagnostics of balance, we analyze the degree of balance by the method devised in *Molemaker et al.* [2005] (Section 5 and Appendix C). We define the streamfunction $\psi$ and the velocity potential $\chi$ as

$$u = -\frac{\partial \psi}{\partial y} + Ro\frac{\partial \chi}{\partial x} \quad \text{and} \quad v = \frac{\partial \psi}{\partial x} + Ro\frac{\partial \chi}{\partial y},$$

and decompose the fluctuation variables $X'$ into balanced and unbalanced components, $X' = X'_{\text{bal}} + X'_{\text{unb}}$. The balanced component satisfies the following diagnostic constraints in Balanced Equations:

$$\left\{\begin{aligned} 2ik\overline{U}_z\hat{\psi} + (2ilRo\overline{U}_z + \frac{\partial}{\partial z})\hat{\chi} + (\frac{ilRo\overline{U}_{zz}}{k^2+l^2} - 1)\hat{w} &= 0 \\ \hat{\psi} &= \hat{p} \\ \hat{b} &= \frac{\partial \hat{p}}{\partial z} \\ (k^2+l^2)\hat{\chi} &= \frac{\partial \hat{w}}{\partial z}\,. \end{aligned}\right. \tag{3.3}$$

The first equation is a combination of the zonal momentum equation, $(ik\overline{U} + \sigma)(k^2 + l^2)\hat{\psi} + (k^2 + l^2)\hat{\chi} + ilRo\overline{U}_z\hat{w} = 0$, and the buoyancy equation, $ik\overline{U}_z\hat{\psi} + ilRo\overline{U}_z\hat{\chi} - \hat{w} - (ik\overline{U} + \sigma)\hat{b} = 0$, by eliminating $\sigma$. The equations (3.3) is a set of higher-order Balanced Equations (which neglects terms of order $Ro^2$). Then the full solution is projected onto the Balanced Equations to maximize the balanced component. Here energy $E' = \int \frac{1}{2}(\overline{u'^2} + \overline{v'^2} + \lambda^2 Ro^2\overline{w'^2} + \overline{b'^2})$ is chosen as a metric for unbalance, and the degree of unbalance $\delta$ is defined by the integrated energy ratio,

$$\delta = \frac{\frac{1}{2}\int [\overline{(u'_{\text{unb}})^2} + \overline{(v'_{\text{unb}})^2} + \lambda^2 Ro^2\overline{(w'_{\text{unb}})^2} + \overline{(b'_{\text{unb}})^2}]\,dz}{\frac{1}{2}\int\, [\overline{u'^2} + \overline{v'^2} + \lambda^2 Ro^2\overline{w'^2} + \overline{b'^2}]\,dz},$$

where the overhead bar denotes horizontal average in both the $x$ and $y$ directions.

In the Boussinesq equations, the kinetic energy for the fluctuation is defined by $\text{KE} = \frac{1}{2}\int(\overline{u'^2} + \overline{v'^2} + \lambda^2 Ro^2\overline{w'^2})$, and the available potential energy is $\text{APE} = \frac{1}{2}\int \overline{b'^2}$.

From (3.1), we derive the energy balance equations for a mean flow $\overline{U}(z)$:

$$\begin{cases} \dfrac{d\text{KE}}{dt} = \displaystyle\int \left[ -Ro\overline{U}_z\overline{u'w'} + \overline{w'b'} \right] dz \\ \dfrac{d\text{APE}}{dt} = \displaystyle\int \left[ \overline{U}_z\overline{v'b'} - \overline{w'b'} \right] dz \,. \end{cases} \tag{3.4}$$

The term $\int -Ro\overline{U}_z\overline{u'w'}$ is the vertical Reynolds stress work, indicating the vertical energy conversion from the mean kinetic energy to the fluctuation kinetic energy (KMKE); the term $\int \overline{U}_z\overline{v'b'}$ is the horizontal buoyancy flux work, indicating the energy transfer from the mean potential energy to the fluctuation potential energy (PMPE). $\int \overline{w'b'}$ represents the energy conversion between the potential and kinetic energy in the fluctuation; a positive value indicates an energy transfer from potential to kinetic.

The growth rate, degree of unbalance $\delta$, potential and kinetic energy conversion from the mean flow, and the eigemode patterns for a BCI mode is shown in Fig. 3.3. The fluctuation variables are normalized by the square root of the integrated energy $\sqrt{E'}$, in both the eigenmode pattern plots, and the calculation of the energy conversions. Three particular $(k, l)$ pairs are chosen near $l = 0$, where the classic BCI is the strongest. The instability exists at a $Ro \rightarrow 0$ limit, and its growth rate slightly increases with $Ro$. The mode is balanced for small $Ro$. Although the unbalanced component increases with $Ro$, it remains small even for intermediate $Ro$. In the quasigeostrophic regime, the mean potential energy conversion (PMPE) is the dominant energy source for the BCI fluctuation to grow. When $Ro$ increases, the contribution of the mean kinetic energy conversion (KMKE) increases, but it is still less than that of the mean potential energy conversion. In the eigenmode patterns, $u'$ has a very small magnitude due to the geostrophic balance. The fluctuation $v'$ is mostly in phase with $b'$, while the phase correlation between $u'$ and $w'$ is weak, which indicates a dominance of PMPE for the BCI mode. As in a quasigeostrophic solution, the streamfunction (not shown in Fig. 3.3, but can be inferred from $u'$ and $v'$) indicates an upstream (westward) phase tilt with height to allow $w'b' > 0$ [*Pedlosky*, 1982].

The characteristics of the CI are demonstrated in Fig. 3.4, for three different $l$

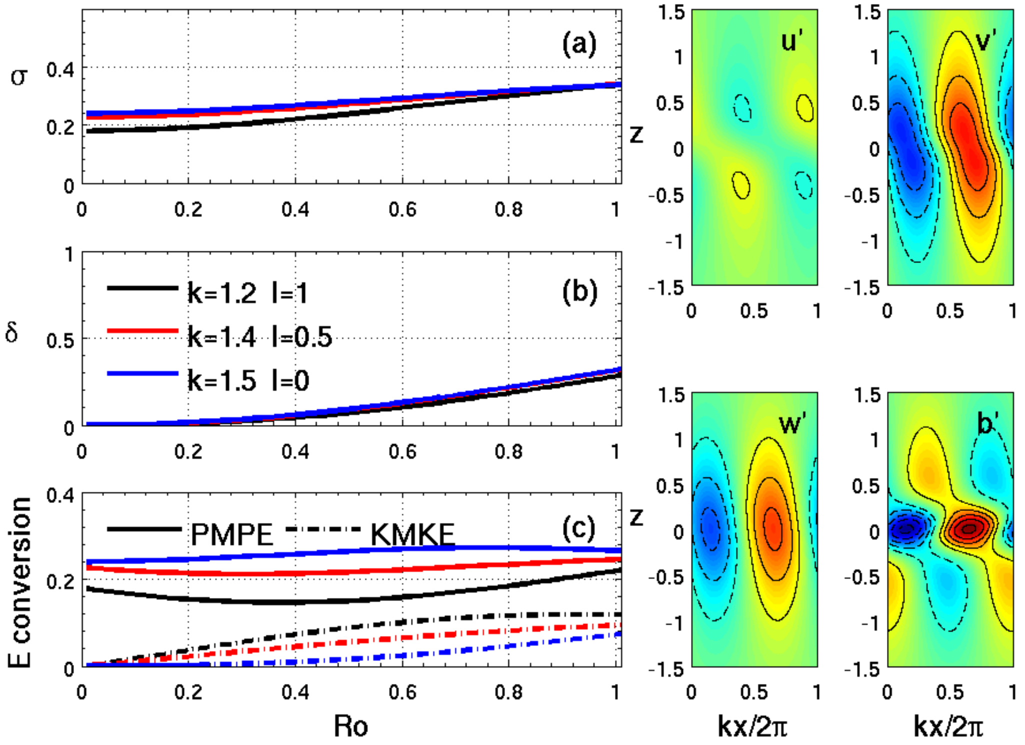

Figure 3.3: Diagnostics and eigenmode patterns for the classic baroclinic instability (BCI) mode (vertically symmetric) in the TANH flow. The left plots are (a) the growth rate, (b) the unbalanced fraction in the total fluctation energy $\delta$, and (c) the energy conversion from mean potential energy (PMPE, solid lines) and mean kinetic energy (KMKE, dash-dot lines) varying with $Ro$, respectively. Three particular $(k,l)$ groups are shown, the black indicates $k = 1.2$, $l = 1$, the red indicates $k = 1.4$, $l = 0.5$, and the blue indicates $k = 1.5$, $l = 0$ in (a), (b) and (c). The right plots are the normalized eigenmode patterns ($u'$, $v'$, $w'$, $b'$) of a BCI mode for $k = 1.5$, $l = 0$, and $Ro = 0.5$, with the same color scale. Red (solid contours) indicates positive, and blue (dashed contours) indicates negative. The contour values start from 0.5, and the interval is 0.5.

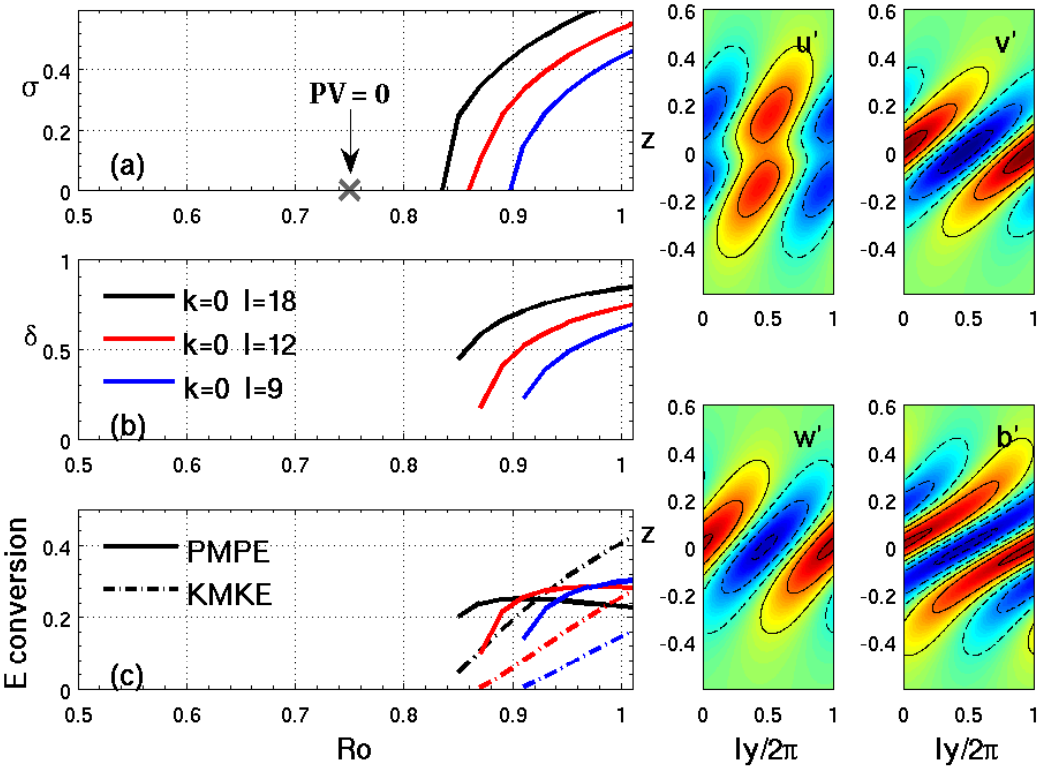

Figure 3.4: Diagnostics and eigenmode patterns for the centrifugal instability (CI) mode (vertically symmetric) in the TANH flow. The plot conventions are the same as in Fig. 3.3. In the left plots, the black indicates $k = 0$, $l = 18$, the red indicates $k = 0$, $l = 12$, and the blue indicates $k = 0$, $l = 9$. The eigenmodes are for $k = 0$, $l = 9$, and $Ro = 1.0$. The cross in (a) indicates the $Ro$ where $PV = 0$. The contour values start from 0.5, and the interval is 1.

values at $k = 0$. CI starts to occur when $PV$ (here $PV$ means $PV_{Ertel}$, and we use $PV$ hereafter) becomes negative, and its growth rate strongly increases with $Ro$. In the TANH flow, the onset criterion for the CI is $Ro > 0.75$ (Table. 3.1). For a fixed $Ro$, there is a lower limit in $l$ for the occurrence of CI, and the growth rate increases with $l$. For $Ro$ slightly larger than 0.75, the CI occurs above very large $l$ ($> 25$); as $Ro$ increases, the lower $l$ limit decreases. Therefore for the $l$ values shown in Fig. 3.4, CI does not yet begin to appear around $Ro = 0.75$. Consistent with the *Stone* [1966] result, the unstable CI mode extents to $l \to \infty$ in non-viscous case. The CI mode is highly unbalanced for intermediate $Ro$. Among the variables, $v'$ and $w'$ have the largest unbalanced fraction, which implies a strong inertial momentum balance in zonal direction, and a large amount of horizontal divergence. The main energy source for a CI mode is the mean potential energy conversion at relatively small $Ro$ or $l$. As $Ro$ or $l$ increases, the mean kinetic energy conversion becomes important and dominant. Similar conclusions on the energetics can be deduced from the analytical solution in *Hoskins* [1974], for the symmetric instability of a uniform vertical shear flow. The phase correlation between $u'$ and $w'$, or $v'$ and $b'$, necessary for positive KMKE or PMPE, is not easily identified in the eigenmode patterns, with both in-phase and out-of-phase components.

The AI1 (Fig. 3.5) appears in a continuous transformation between BCI and CI, and it does not clearly separate from the BCI and CI in ($k$, $l$). However, it behaves differently from the other two classic instabilities. It is an ageostrophic instability that occurs at a finite $Ro$, between the $Ro$ regimes where BCI and CI exist. Due to the obscurity of its separation with BCI or CI, the onset $Ro$ for the AI1 mode depends on ($k$, $l$), thus is not clearly determined, but it is close to 0.53 ($A\text{-}S = 0$), and smaller than 0.75 ($PV = 0$), which allows its categorization as a type of AAI. The strongest unstable AI1 mode in a ($k$, $l$) space occurs far from $l = 0$ or $k = 0$. The mode is mostly balanced for the $Ro$ as it begins to occur, but the unbalanced component strongly increases with $Ro$. Distinguished from the BCI and CI, the mean kinetic energy conversion is the main energy

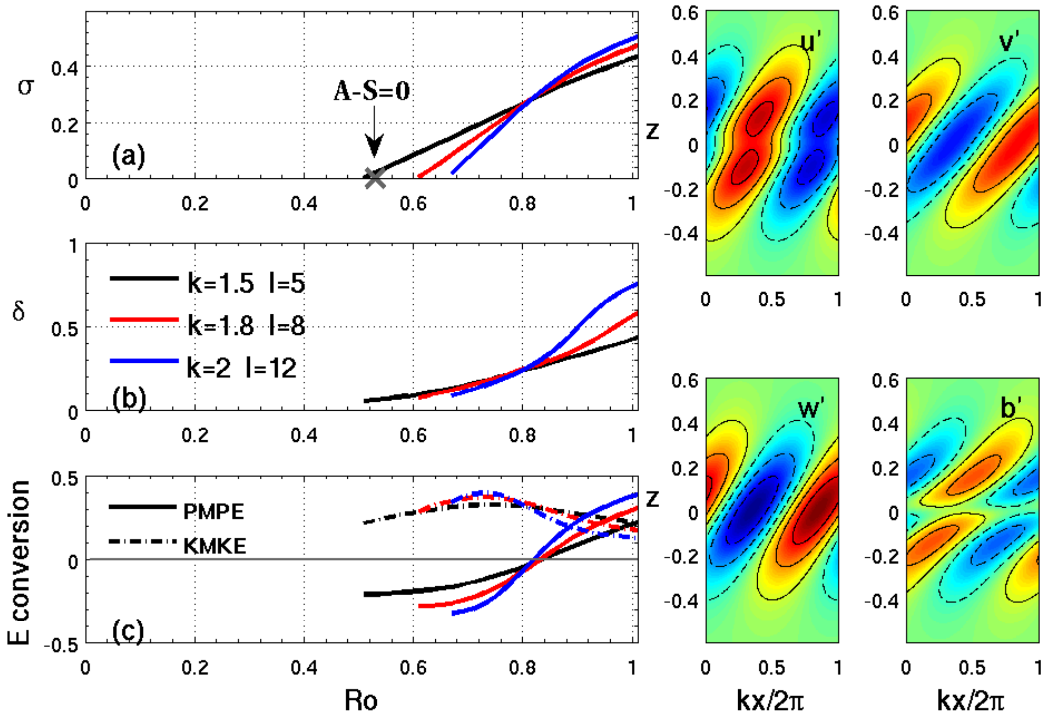

Figure 3.5: Diagnostics and eigenmode patterns for the first type of ageostrophic instability (AI1) mode (vertically symmetric) in the TANH flow. The plot conventions are the same as in Fig. 3.3. In the left plots, the black indicates $k = 1.5$, $l = 5$, the red indicates $k = 1.8$, $l = 8$, and the blue indicates $k = 2.0$, $l = 12$. The eigenmodes are for $k = 1.8$, $l = 8$, and $Ro = 0.7$. The cross in (a) indicates the $Ro$ where $\overline{A}$-$\overline{S} = 0$. The contour values start from 0.5, and the interval is 1.

source for the unstable fluctuation in AI1, while the mean potential energy conversion is negative for intermediate *Ro*, indicating a kinetic energy conversion to potential energy in the fluctuation fields. The evidence is also shown in the eigenmode patterns: there is a $180^{\mathrm{o}}$ phase shift between $w'$ and $b'$. $u'$ and $w'$ are positively correlated, and $v'$ and $b'$ are negatively correlated. In a $(k, l)$ space for $Ro = 0.8$, where CI just starts to occur and is confined near $k = 0$, it is clear that the potential energy conversion is positive near both $k = 0$ and $l = 0$ (where the BCI is strongest), and it is negative with a minimum around $k = 2$ for intermediate $l$; the negative potential energy conversion region roughly encloses the $(k, l)$ regime for AI1. For $Ro = 1$, or even larger values, the CI extends to the larger-$k$ direction; AI1 and CI become less distinguishable in $(k, l)$.

Because we study the mean flow with a very small $\lambda = 0.01$, all the unstable modes discussed above are mostly hydrostatic, although there is a small unbalanced fraction in the $b'$ field.

## 3.3 AI2: The Ageostrophic Modes Associated with ICL

Besides the joint zero-frequency unstable modes discussed in Sec. 3.2, we find some other ageostrophic modes in the TANH and DJET flows, which all appear with inertial critical layers (ICL). The inertial critical layer is defined as where $\overline{U}(z) - Cp = \pm f/k$ dimensionally, or $\overline{U}(z) - Cp = \pm 1/Rok$ non-dimensionally, where $Cp = \omega/k$ is the downstream phase speed. The physical characteristics of ICL have been recognized as an "absorber" of inertia-gravity waves, and it is indicated that inertia-gravity waves in ICL may be unstable due to a non-uniform mean flow background [*Jones*, 1967, *Yamanaka*, 1985]. We categorize these modes as another type of ageostrophic instability: AI2. In all, AI2 has a weaker growth rate than AI1. With $\lambda = 0.01$, AI2 is also mostly hydrostatic.

The EADY ageostrophic instability has been interpreted as a coupling between an edge wave and an inertia-gravity wave, which occurs with an inertial critical layer

[*Nakamura*, 1988, *Plougonven et al.*, 2005], and hence is categorized as AI2 in this paper. We name the AI2 that couples balanced shear waves and inertia-gravity waves as a BG mode ("B" refers to balanced shear waves, and "G" refers to inertia-gravity waves), and the AI2 that couples two inertia-gravity waves as a GG mode. The EADY ageostropic instability is of the BG type, but special due to its dependence on the vertical boundaries. For a $f$-plane vertical shear $\overline{U}(z)$, the horizontal gradient of $PV$ is

$$PV_y = -Ro\overline{U}_{zz}\,; \tag{3.5}$$

a non-zero $PV_y$ ($\overline{U}_{zz}$) supports the existence of a balanced shear wave (Rossby wave). The EADY flow has a zero interior $PV_y$, but the horizontal buoyancy gradient (proportional to $\overline{U}_z$) at the vertical boundaries supports the existence of edge waves, which is a special type of balanced wave. In the EADY flow, there are no interior shear waves, so the vertical boundary is essential for the occurrence of an unstable BG mode. If we consider a flow transformation from EADY to TANH, $\overline{U}_z$ gradually vanishes at the boundaries and $PV_y$ ($\overline{U}_{zz}$) begins to appear in the interior of the vertical shear flow. The classic BCI would still exist due to the appearance of interior $PV_y$. Then how about the AI2? An experiment is designed to examine the change of the ageostrophic instability in the transformation. We study a series of hyperbolic tangent mean flows,

$$\overline{U}(z) = \frac{1}{a}\tanh(az)\,, \tag{3.6}$$

in a fixed domain [-0.5 0.5]. The mean flows have a parameter $a$ to control their shapes and $\overline{U}_z$ values at the boundaries. All the mean flows are normalized to have the same $\overline{U}_z = 1$ at $z = 0$. When $a \rightarrow 0$, the flow becomes an EADY flow and $\overline{U}_z = 1$ at the boundaries. As $a$ increases, $\overline{U}_z$ vanishes at the boundaries and the interior $PV_y$ ($\overline{U}_{zz}$) increases. The upper plots in Fig. 3.6 show the growth rate of the BG mode for the mean flows with $\overline{U}_z = 1$ and $\overline{U}_z = 0.9$ at the boundaries, respectively. The BG mode separates in $k$ when $\overline{U}_z$ decreases; the right part occurs towards larger and larger $k$ while the left persists in the same $k$ range. The growth rates of both parts decrease dramatically with decreasing $\overline{U}_z$. The maximum growth rate for the BG mode in $k <$

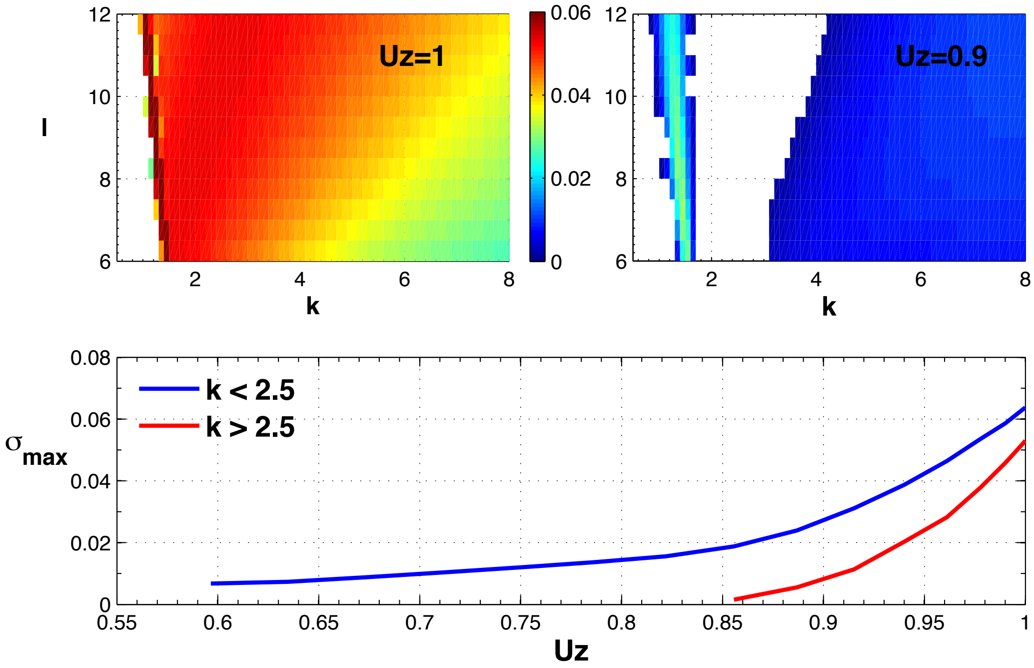

Figure 3.6: The BG mode vanishes in the EADY slow as $\overline{U}_z$ decreases at the boundaries due to the increase of $a$ in (3.6). The upper plots demonstrate the growth rate $\sigma(k, l)$ in the BG mode for $\overline{U}_z = 1$ ($a = 0$) and $\overline{U}_z = 0.9$ ($a = 0.65$), respectively, with the same color scale. The lower plot shows the maximum growth rate versus the boundary $\overline{U}_z$ for $k < 2.5$ (blue) and $k > 2.5$ (red), respectively.

2.5 and $k > 2.5$ versus $\overline{U}_z$ is shown in the lower plot. In both $k$ ranges, the BG mode vanishes when $\overline{U}_z$ decreases, with the large-$k$ BG mode vanishing more quickly. When $\overline{U}_z$ vanishes, the edge wave no longer exists, therefore the EADY BG mode disappears. However, different from the BCI, no other BG mode arises with increasing interior $PV_y$ in the hyperbolic tangent flows, even for a large value of $a$, where the interior shear wave replaces the edge wave in the TANH flow.

Through a coupling of an interior shear wave and an inertia-gravity wave, the BG mode is found in the DJET flow. Figure 3.7 shows the fluctuation steam-function pattern for the BG mode in the DJET flow. The mode appears with an inertial critical layer and clearly consists of two components. Near the ICL, the mode is highly unbalanced and confined near the ICL; this is the inertia-gravity wave component. The balanced component, an interior shear wave, is in the mean shear region. It is supported by the outer $PV_y$ in the velocity roll-off region that does not exist in the TANH flow. The structure of this BG mode is very similar to that in the EADY flow (Fig. 7 in *Molemaker et al.* [2005]), except for the vertical location of the shear wave. Different from the EADY BG mode, this interior BG mode only occurs at small and intermediate $k$. The growth rate of this BG mode in a ($k$, $l$) space for $Ro = 0.01$ and $Ro = 1$ is shown in Fig. 3.8. At $Ro = 0.01$, there is a BCI mode near $l = 0$ with non-zero frequency. The mode is balanced and the energy conversion is from potential to kinetic. Like AI1, the BG type AI2 in the DJET flow also comes from a continuous transformation. As $Ro$ increases, this mode expands to intermediate $k$ and $l$ with an increasing growth rate; the inertia-gravity wave begins to couple with the shear flow, and an ICL appears at intermediate ($k$, $l$). At $Ro = 1$, the mode has expanded to large $l$ and it is unbalanced by a coupling with inertia-gravity waves for all the intermediate and large ($k$, $l$) region. Figure 3.8(c) shows the growth rate versus $Ro$ for three particular pairs of ($k$, $l$). The BG mode starts to occur in the neighborhood of $A\text{-}S = 0$ and below the $Ro$ onset of CI, hence can also be categorized as AAI. The main energy source for this interior BG mode is the mean kinetic energy.

In the TANH flow, we find a type of AI2 that can be interpreted as a coupling of two inertia-gravity waves; we call it as a GG mode. The characteristics of this mode is shown in Fig. 3.9. It appears at intermediate $k$ and large $l$. The mode is mostly hydrostatic and starts to appear around $Ro \sim 0.8$, far below the onset $Ro$ of KHI ($Ro = 1.51$). It is highly unbalanced for intermediate $Ro$, including all the fluctuation velocities $u'$, $v'$ and $w'$. An unstable GG mode grows by drawing energy from the available potential energy of the mean flow, and the instability transfers the fluctuation kinetic energy to the mean state kinetic energy. A GG mode has two inertial critical layers (indicated by the horizontal black lines in the patten plots), with two inertia-

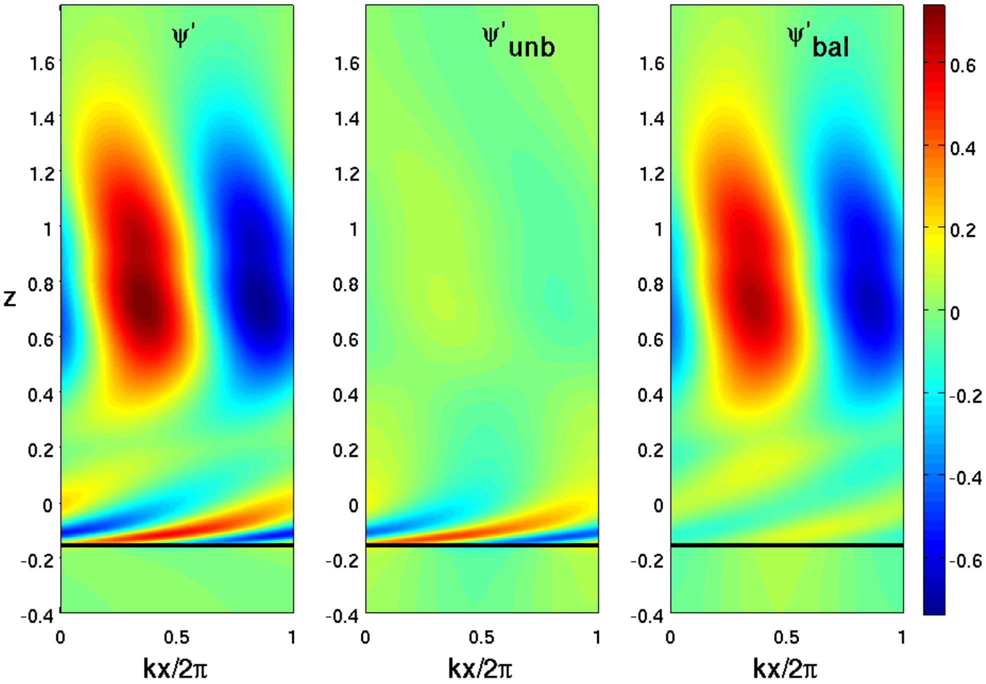

Figure 3.7: The fluctuation streamfunction patterns of a BG mode (full, unbalanced, and balanced components, with the same color scale) for $k = 1.8$, $l = 3.5$, and $Ro = 1$. The black horizontal lines indicate the inertial critical layers.

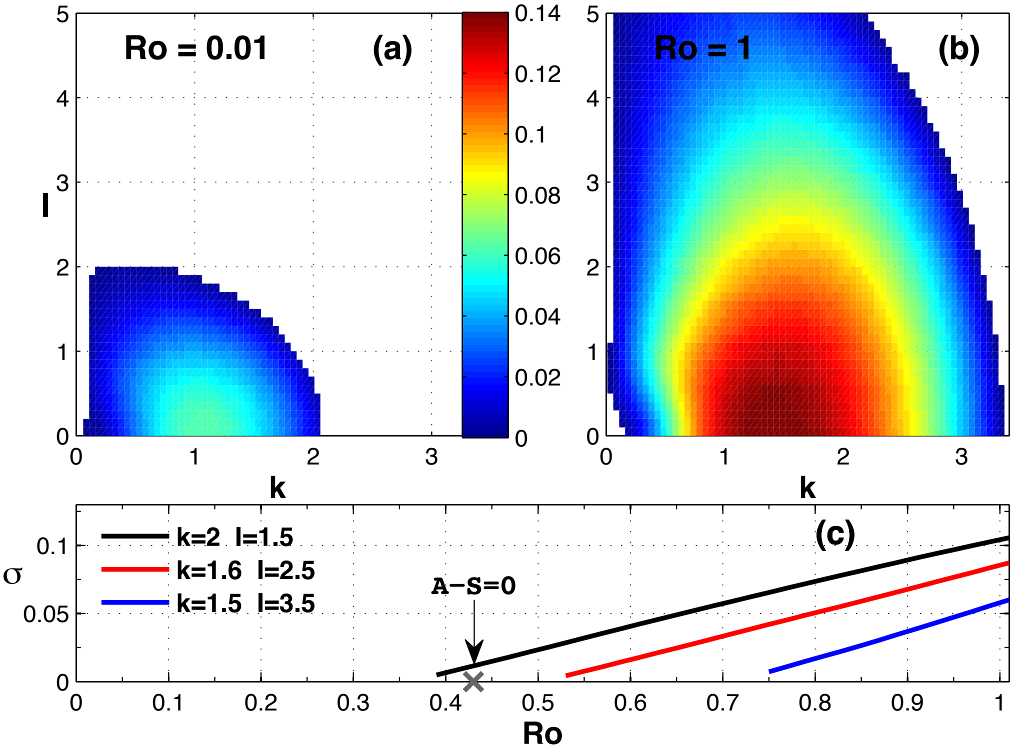

Figure 3.8: The growth rate of the BG mode in the DJET flow in a (*k*, *l*) space is shown for *Ro* = 0.01 (a) and *Ro* = 1 (b). (c) shows the growth rate versus *Ro* for three particular (*k*, *l*) pairs. The black indicates *k* = 2, *l* = 1.5, the red indicates *k* = 1.6, *l* = 2.5, and the blue indicates *k* = 1.5, *l* = 3.5. The cross indicates the *Ro* where $\overline{A}$-$\overline{S}$ =0.

gravity wave components confined near them. The component sheared inertia-gravity waves are Doppler-shifted to have the same frequency. The GG mode shown in Fig. 3.9 has a zero frequency; there are other GG modes with non-zero frequencies and non-symmetric vertical structures.

All the AI2 modes (including BG and GG) have inertial critical layers and hence are associated with the coupling of inertia-gravity waves. The BG mode occurs near the *Ro* where $A\text{-}S = 0$, therefore is an AAI in type; the GG mode arises away from this condition, hence is not associated with it. We do find a type of vertically asymmetric mode ($\omega \neq 0$) in the TANH flow, with a weak growth rate ($\sim 0.01$), occurring at intermediate $k$ and large $l$ for *Ro* values above the CI threshold ($> 0.8$). It is also an unbalanced instability, whose energy source is the mean potential energy. It does not appear with an ICL, and is neither AI1 nor AI2.

Because of the continuous transformation of mode characteristics in ageostrophic instability, rather than arising with a distinct separation from other types of instability, there is not unique definition of a representative growth rate for either AI1 or AI2 at a fixed *Ro*. In Sec. 3.2 and 3.3, the growth rate dependence on *Ro* is shown for several $(k, l)$ pairs, which do indicate the relevance of the $A\text{-}S$ condition as a neighborhood for onset of instability.

## 3.4 Main Conclusions

We solve the linear instability problem for an interior, baroclinic shear flow $\overline{U}(z)$ in a 3D, rotating, continuously stratified fluid. Two types of mean flow are examined: TANH (hyperbolic tangent flow) and DJET (double-jet flow), with a focus on the TANH flow. We find two types of baroclinic, ageostrophic instability, both of which are mostly hydrostatic with the small aspect ratio $\lambda$. For a particular $l$ (cross-stream wavenumber), they start to occur at finite *Ro*, and their growth rate increases with increasing *Ro*. The first type of ageostrophic instability (AI1) comes from a continuous transformation and

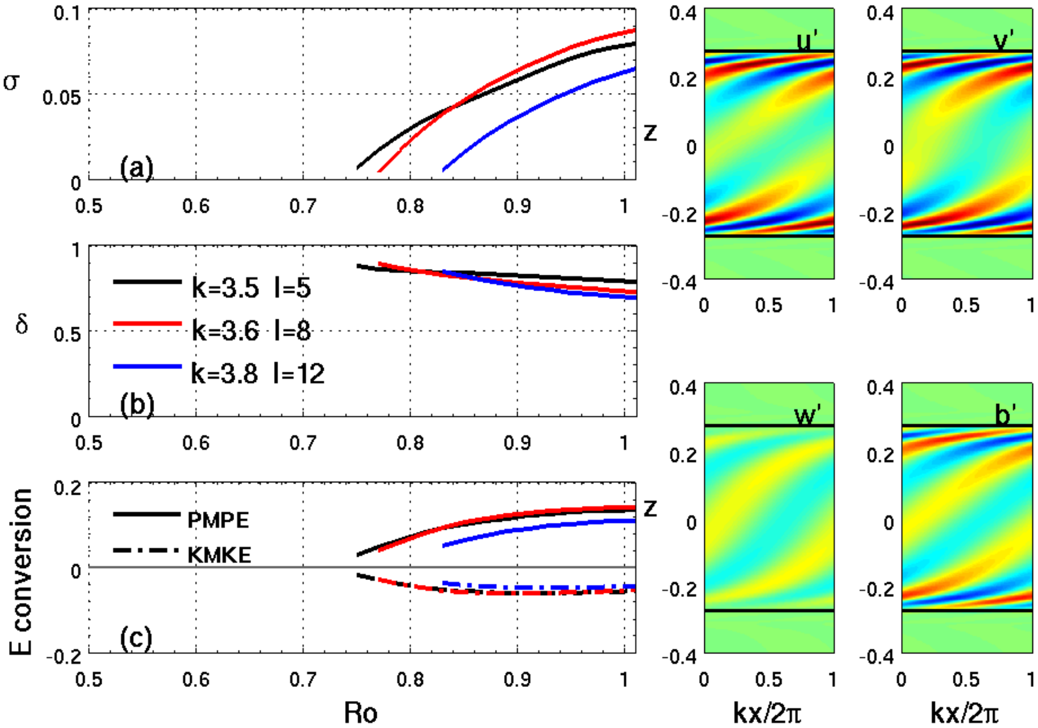

Figure 3.9: The diagnostics and eigenmode patterns for the second type of ageostrophic instability (AI2) of the GG type in the TANH flow. The plot conventions are the same as in Fig. 3.3, except that the inertial critical layers are indicated by the black horizontal lines right plots. In the left plots, the black indicates $k$ = 3.5, $l$ = 5, the red indicates $k$ = 3.6, $l$ = 8, and the blue indicates $k$ = 3.8, $l$ = 12. The eigenmodes are for $k$ = 3.8, $l$ = 12, and $Ro$ = 0.85. The contour values start from 1, and the interval is 1.

expansion in ($k$, $l$) between the classic baroclinic instability (BCI) and centrifugal instability (CI). It occurs between the *Ro* regimes for BCI and CI, and in the ($k$, $l$) range that is far from $k = 0$ or $l = 0$. The AI1 mode is mostly balanced for the *Ro* at which it starts to occur, and it is unbalanced for intermediate *Ro*. Unlike the BCI and CI, the main energy source for AI1 is the mean kinetic energy, and the unstable fluctuation transfers energy to the mean potential energy. This mode is also found in the EADY flow, except in a narrower band of $k$. The second type of ageostrophic instability (AI2) is associated with inertial critical layers and hence related to a coupling with inertia-gravity waves. The coupling is either between a balanced shear wave and an inertia-gravity wave (BG type), or between two inertia-gravity waves (GG type). The EADY ageostrophic instability is caused by a coupling between an edge wave and an inertia-gravity wave, and it is an AI2 of the BG type. In a transformation from a EADY to TANH flow, the BG mode in the EADY flow disappears with vanishing $\overline{U}_z$ (proportional to the horizontal buoyancy gradient) at boundaries, while no other BG mode that is associated with an interior potential vorticity gradient arises with increasing interior $\overline{U}_{zz}$ (proportional to $PV_y$) in the TANH flow. The BG mode is found in the DJET flow, as a coupling between an interior shear wave and an inertia-gravity wave. It appears with an inertial critical layer, and the balanced and unbalanced components are clearly identified in the fluctuation patterns. In the TANH flow, we find the AI2 of a GG type. The main energy source for an AI2 BG mode is the mean kinetic energy, while that for an AI2 GG mode is the mean potential energy. Both AI1 and AI2 are unbalanced instabilities, with the growth rate of AI2 generally less than AI1.

Both AI1 and AI2 of the BG type in the interior $\overline{U}(z)$ flows occur in the neighborhood of $A\text{-}S = 0$, hence are possibly in the AAI category. As other AAI modes in the previous literature, they do not have a sharp onset criterion. The AI2 of GG type occurs for a *Ro* value beyond the $A\text{-}S$ condition, and therefore it is not a type of AAI. The characteristics of the AI1 and AI2 modes are not the same, and they are not the same as other AAI modes previously found in other flows (Sec. 1.2), including the EADY flow.

This indicates that AAI is more a collection of unstable mode types rather than a single unique type. AI1 does not have evident inertia-gravity wave characteristics (radiation or inertial critical layers), but AI2 does, indicating not all the unbalanced instabilities and loss of balance in a continuously stratified flow are related to an energy transfer to inertia-gravity waves. Unlike the ageostrophic instability in the EADY flow, both AI1 and AI2 do not require boundaries. Both instabilities are absent in the quasigeostrophic limit ($Ro \to 0$) and distinct from BCI, and they start to occur below the $Ro$ criteria for CI and KHI. The understanding of these types of ageostrophic instability demonstrates a possible local route for the loss of balance and forward energy cascade in the interior ocean and atmosphere.

# CHAPTER 4

# Summary and Discussion

## 4.1 Summary

This dissertation mainly contains two parts: the ageostrophic instability of a horizontal shear flow in rotating shallow water equations, and the ageostrophic instability of a vertical shear flow in 3D stratified fluids. The purpose of our work is to look for general types of ageostrophic instability that can provide a local route to a loss of balance in the interior oceanic and atmospheric flows, which leads to an efficient energy transfer towards small scales and final dissipation. As an approach, the linear instability problems of continuously differentiable, interior $\overline{U}(y)$ and $\overline{U}(z)$ without boundaries or surface outcropping are solved in rotating shallow water equations and Boussinesq equations, respectively.

In a rotating shallow-water, interior barotropic shear flow $\overline{U}(y)$, there are mainly two types of neutral modes: balanced shear wave mode (B mode) and inertia-gravity wave mode (G mode). The resonant coupling of two neutral modes yields three types of instability: B-B, B-G and G-G. B-B instability is the balanced shear instability (classic barotropic instability) that relates to Rayleigh's inflection point condition. Both B-G and G-G are unbalanced instabilities, which are highly ageostrophic and occur when the local $\tilde{Fr}$ is sufficiently large (associated with the second stability condition of *Ripa* [1983]). The resonant G component can be clearly identified in the ageostrophic instabilities. However, the B-G instability involves a set of B modes due to a continuously varying potential vorticity gradient, so its resonant B component is less evident in the unstable modes. The balanced instability is suppressed by large $Fr$, while the growth rate of the ageostrophic instability increases with increasing $Fr$. We examine four types of mean flow (Bickley jet, cyclonic and anticyclonic double jet, and triple jet); it is found that the strength of the ageotrophic instabilities also depends on the shape of the mean flow. In the nonlinear vortex dynamics, the ageostrophic instability is manifested in the time evolution of a finite $Ro$ modon, appearing in the cyclone region, where the local $\tilde{Fr}$ is large.

In a rotating, continuously stratified, interior baroclinic shear flow $\overline{U}(z)$, we find two types of baroclinic, ageostrophic instability. They start to occur at finite $Ro$, and their growth rate increases with increasing $Ro$. The first type of ageostrophic instability (AI1) comes from a continuous transformation and expansion in $(k, l)$ between the classic baroclinic instability (BCI) and centrifugal instability (CI). It occurs between the $Ro$ regimes for BCI and CI, and in the $(k, l)$ range that is far from $k = 0$ or $l = 0$. The AI1 mode is mostly balanced for the $Ro$ at which it starts to occur, and it is unbalanced for intermediate $Ro$. The main energy source for AI1 is the mean kinetic energy, and the unstable fluctuation transfers energy to the mean potential energy. The second type of ageostrophic instability (AI2) is associated with inertial critical layers and hence related to a coupling with inertia-gravity waves. The coupling is either between a balanced shear wave and an inertia-gravity wave (B-G type), or between two inertia-gravity waves (G-G type). In a transformation from the Eady flow to the hyperbolic tangent flow, the B-G mode in the Eady flow disappears with vanishing $\overline{U}_z$ at boundaries, while no other B-G mode that is associated with an interior potential vorticity gradient arises with increasing interior $PV_y$ in the hyperbolic tangent flow. The B-G mode is found in the double-jet flow, appearing with an inertial critical layer. We find the AI2 of a G-G type in both the hyperbolic tangent and the double-jet flows. The main energy source for an AI2 B-G mode is the mean kinetic energy, while that for an AI2 G-G mode is the mean potential energy. Both AI1 and AI2 of the B-G type in the interior $\overline{U}(z)$ flows occur in the neighborhood of $A\text{-}S = 0$ [*McWilliams et al.*, 1998], hence are possibly in the AAI category. The AI2 of G-G type occurs for a $Ro$ value beyond the $A$-$S$ condition, and therefore it is not a type of AAI.

To summarize existing literature and our results for a general picture of ageostrophic instability, we have learnt the following points:

1. Ageostrophic instability is a generic behavior in interior horizontal and vertical shear flows. The instability occurs or becomes strong at finite $Ro$ and $Fr$ with values smaller than those required for the onset of classic unbalanced types of instability (centrifugal, Kelvin-Helmholtz, gravitational). Ageostrophic instability provides an important local route for the breakdown of balance and forward energy cascade in the interior ocean.

2. Ageostrophic instability formally involves a “resonant” coupling by the mean shear flow of the resting-state linear modes comprised of quasigeostrophic and unbalanced inertia-gravity or Kelvin wave types. In idealized configurations with boundaries or discontinuous interior interfaces, the resonating modes may sometimes readily be identified, but not usually not so with general mean shear profiles and continuous stratification in the interior.

3. Ageostrophic instability in rotating shallow water occurs for a sharp criterion: local $Fr$ exceeds a critical value (Ripa, 1983). In contrast, the ageostrophic instability in continuously stratified flow with $PV > 0$ does not have a sharp onset but for many flows its growth rate strongly increases near the neighborhood of $A - S = 0$ (McWilliams et al., 1998). This difference reflects the lower bound on the vertical scale and inertia-gravity wave speed in rotating shallow water.

4. Looking across many mean flow and stratification configurations, it seems clear that not all interior ageostrophic instabilities are the same. The occurrence and strength of the ageostrophic instability depend on the shape of the mean flow. Anticyclonic, ageostrophic instability (AAI) types are common, but some cyclonic mean flows are unstable with intermediate $Ro$.

## 4.2 Remaining Questions and Future Work

There are still some questions or possible work remaining in the study of ageostrophic instabilities:

1. The study of B-G instability in rotating shallow-water flows indicates that the imprint of the B component is less evident when the mean flow has a continuous potential vorticity gradient rather than a singular potential vorticity. We understand that the continuous potential vorticity gradient supports a series of continuous shear waves, rather than only one in the singular case. However, a direct explanation of why the shear wave component becomes obscure in the unstable mode patterns with a continuous mean potential vorticity gradient is still unclear.

2. We see a B-G type AI2 in both EADY and DJET flows, where the boundary edge wave or interior shear wave couples with an inertia-gravity wave. The TANH flow has an interior potential vorticity gradient that supports the existence of shear waves; however, we do not find a B-G type AI2 in the TANH flow even for a $Ro > 1$. This implies that the occurrence of the B-G AI2 requires some other conditions, e.g., the particular shape of the mean flow. What could be the requirement and associated explanation?

3. All previous AAIs in a 3D stratified flow involve inertia-gravity waves or Kelvin waves. We identify AI1 as a type of AAI, but different from AI2 and previous AAI types. *Ménesguen et al.* [2012] find a transformation of unstable modes near $A - S = 0$. Therefore, AAI is a collection of instabilities rather than a unique type. Can we find other types of AAI in other mean flows? Is there a general wave interpretation (or visual physical interpretation) associated with AAI?

4. In general, the linear instability problem of interior $\overline{U}(y, z)$ shear flows is not fully understood yet. The problem might be solved with a high resolution and various

pairs of *Bu* and *Ro* if the numerical technique is improved and the calculation is allowed in the future.

Following the theoretical study in this dissertation, some work could be done in the next steps in order for a further application of the basic theory.

1. The nonlinear evolution of some parallel shear flows $\overline{U}(y)$ and $\overline{U}(z)$ could be examined in a direct numerical simulation, with a focus on how the balanced motions are broken down by the ageostrophic instabilities, and how the energy is transferred to smaller scales in the nonlinear turbulent process.

2. Some lab experiments could be developed to study the turbulent dynamics in an initially balanced flows with $PV > 0$ for a finite *Ro* like the work in *Le Bars and Le Gal* [2007]. With lab studies on various types of flow, we might be able to get a visual physical understanding on the $A - S$ condition. We expect the experiments could tell us a difference on the turbulence evolution and turbulent energy spectrum among the flows with AAI, the classic ageostrophic flows with CI or KHI, and the classic shear flows with barotropic and baroclinic instabilities.

3. Most of the observation and modeling data in the ocean did not have enough resolution to resolve submesoscale features in the past. In recently years, plenty of new data coming from both observations and regional oceanic simulations is capable to capture the submesoscale phenomena. The existing ageostrophic theories can provide a support for the analysis and understanding of the data.

4. All the studies in 1, 2, 3 can help us for a better understanding of the physics on submesoscale or even smaller scales in the ocean. The understanding of submesoscale dynamics could further apply to improve the parameterization of eddy diffusivity or other small-scale features in GCMs.

5. The large-scale atmosphere of other planets, such as Venus and Titan, manifest strong ageostrophic characteristics. The flows have a finite *Ro* and behaves quite

differently from the fluids on earth, and the quasigeostrophic theory fails. The ageostrophic theory in this dissertation may be applied to discribe the dynamics of the other planetary atmospheres.

# Bibliography

Balmforth, N. J. (1999), Shear instability in shallow water, *J. Fluid Mech.*, *387*, 97–127.

Barth, J. A. (1994), Short-wavelength instabilities on coastal jets and fronts, *J. Geophys. Res.*, *99*, 16,095–16,116.

Boss, E., N. Paldor, and L. Thompson (1996), Stability of a potential vorticity front: from quasi-geostrophy to shallow water, *J. Fluid Mech.*, *315*, 65–84.

Bouchut, F., B. Ribstein, and V. Zeitlin (2011), Inertial, barotropic, and baroclinic instabilities of the Bickley jet in two-layer rotating shallow water model, *Phys. Fluids*, *23*, 126,601.

Bryan, F. (1987), Parameter sensitivity of Primitive Equation Ocean General Circulation Models, *J Phys. Oceanogr.*, *17*, 970–986.

Chandrasekhar, S. (1961), *Hydrodynamic and Hydromagnetic Stability*, Cambridge University Press.

Charney, J. G. (1947), The dynamics of long waves in a baroclinic westerly current, *J. Atmos. Sci.*, *4*, 136–162.

Charney, J. G. (1962), Integration of the Primitive and Balanced Equations, *Proc. Int. Symp. Numerical Weather Prediction*, pp. 131–152.

Charney, J. G. (1971), Geostrophic Turbulence, *J. Atmos. Sci.*, *28*, 1087–1094.

Chelton, D. B., M. G. Schlax, and R. M. Samelson (2011), Global observations of nonlinear mesoscale eddies, *Prog. Oceanogr.*, *91*, 167–216.

de La Cruz-Heredia, M., and G. W. K. Moore (1999), Barotropic instability due to Kelvin wave-Rossby wave coupling, *J. Atmos. Sci.*, *56*, 2376–2383.

Drazin, P. G., and W. H. Reid (1981), *Hydrodynamic Stability*, Cambridge University Press.

Dritschel, D. G., and J. Vanneste (2006), Instability of a shallow-water potential-vorticity front, *J. Fluid Mech.*, *561*, 237–254.

Eady, E. T. (1949), Long waves and cyclone waves, *Tellus*, *1*, 33–52.

Ferrari, R., and C. Wunsch (2010), The distribution of eddy kinetic and potential energies in the global ocean, *Tellus A*, *62*, 92–108.

Gargett, A. (1984), Vertical eddy diffusivity in the ocean interior, *J. Mar. Res.*, *42*, 359–393.

Griffiths, R. W., P. D. Killworth, and M. E. Stern (1982), Ageostrophic instability of ocean currents, *J. Fluid Mech.*, *117*, 343–377.

Gula, J., and V. Zeitlin (2010), Instabilities of buoyancy-driven coastal currents and their nonlinear evolution in the two-layer rotating shallow water model. Part 1. Passive lower layer, *J. Fluid Mech.*, *659*, 69–93.

Gula, J., R. Plougonven, and V. Zeitlin (2009a), Ageostrophic instabilities of fronts in a channel in a stratified rotating fluid, *J. Fluid Mech.*, *627*, 485.

Gula, J., V. Zeitlin, and R. Plougonven (2009b), Instabilities of two-layer shallow-water flows with vertical shear in the rotating annulus, *J. Fluid Mech.*, *638*, 27.

Gula, J., V. Zeitlin, and F. Bouchut (2010), Instabilities of buoyancy-driven coastal currents and their nonlinear evolution in the two-layer rotating shallow water model. Part 2. Active lower layer, *J. Fluid Mech.*, *665*, 209–237.

Hayashi, Y. Y., and W. R. Young (1987), Stable and unstable shear modes of rotating parallel flows in shallow waters, *J. Fluid Mech.*, *184*, 477–504.

Held, I. M. (1985), Pseudomomentum and the orthogonality of modes in shear flows, *J. Atmos. Sci.*, *42*, 2280–2288.

Hoskins, B. J. (1974), The role of potential vorticity in symmetric stability and instability, *Q. J. Roy. Meteor. Soc.*, *100*, 480–482.

Iga, K. (1999), Critical layer instability as a resonance between a non-singular mode and continuous modes, *Fluid Dyn. Res.*, *25*, 63–86.

Jones, W. L. (1967), Propagation of internal gravity waves in fluids with shear flow and rotation, *J. Fluid Mech.*, *30*, 439–448.

Killworth, P., N. Paldor, and M. Stern (1984), Wave propagation and growth on a surface front in a two-layer geostrophic current, *J. Mar. Res.*, *42*, 761–785.

Kizner, Z., G. Reznik, B. Fridman, R. Khvoles, and J. McWilliams (2008), Shallow-water modons on the f-plane, *J. Fluid Mech.*, *603*, 305–329.

Kubokawa, A. (1985), Instability of a geostrophic front and its energetics, *Geophys. Astro. Fluid*, *33*, 323–357.

Kubokawa, A. (1986), Instability caused by the coalescence of two modes of a one-layer coastal current with a surface front, *J. Oceanogr.*, *42*, 373–380.

Lahaye, N., and V. Zeitlin (2012), Shock modon: A new type of coherent structure in rotating shallow water, *Phys. Rev. Lett.*, *108*(4), 044502.

Lambaerts, J., G. Lapeyre, and V. Zeitlin (2011), Moist versus dry barotropic instability in a shallow-water model of the atmosphere with moist convection, *J. Atmos. Sci.*, *68*, 1234–1252.

Le Bars, M., and P. Le Gal (2007), Experimental analysis of the stratorotational instability in a cylindrical Couette flow, *Phys. Rev, Lett.*, *99*(6), 064502.

Lin, C. C. (1961), Some mathematical problems in the theory of the stability of parallel flows, *J. Fluid Mech.*, *10*, 430–438.

Lorenz, E. (1960), Energy and numerical weather prediction, *Tellus*, *12*, 364–373.

McWilliams, J. (1981), Numerical studies of barotropic modons, *Dynam. Atmos. Oceans*, *5*, 219–238.

McWilliams, J. C., and I. Yavneh (1998), Fluctuation growth and instability associated with a singularity of the balance equations, *Phys. Fluids*, *10*, 2587–2596.

McWilliams, J. C., I. Yavneh, M. J. P. Cullen, and P. R. Gent (1998), The breakdown of large-scale flows in rotating, stratified fluids, *Phys. Fluids*, *10*, 3178–3184.

McWilliams, J. C., M. J. Molemaker, and I. Yavneh (2004), Ageostrophic, anticyclonic instability of a geostrophic, barotropic boundary current, *Phys. Fluids*, *16*, 3720–3725.

Mechoso, C. R., and D. M. Sinton (1983), On the energy analysis of the two-layer frontal model., *J. Atmos. Sci.*, *40*, 2069–2074.

Ménesguen, C., J. C. McWilliams, and M. J. Molemaker (2012), Ageostrophic instability in a rotating stratified interior jet, *J. Fluid Mech.*, *In press.*

Miles, J. W. (1961), On the stability of heterogeneous shear flows, *J. Fluid Mech.*, *10*, 496–508.

Molemaker, M. J., J. C. McWilliams, and I. Yavneh (2001), Instability and equilibration of centrifugally stable stratified Taylor-Couette flow, *Phys. Rev. Lett.*, *86*, 5270–5273.

Molemaker, M. J., J. C. McWilliams, and I. Yavneh (2005), Baroclinic instability and loss of balance, *J. Phys. Oceanogr.*, *35*, 1505–1517.

Moore, G. W. K., and W. R. Peltier (1987), Cyclogenesis in frontal zones, *J. Atmos. Sci.*, *44*, 384–409.

Moore, G. W. K., and W. R. Peltier (1990), Nonseparable Baroclinic Instability. Part II: Primitive-Equations Dynamics., *Journal of Atmospheric Sciences*, *47*, 1223–1242.

Nakamura, N. (1988), Scale selection of baroclinic instability–effects of stratification and nongeostrophy, *J. Atmos. Sci.*, *45*, 3253–3268.

Ooyama, K. (1966), On the stability of the baroclinic circular vortex: A sufficient condition for instability, *J. Atmos. Sci.*, *23*, 43–53.

Orlanski, I. (1968), Instability of frontal waves., *J. Atmos. Sci.*, *25*, 178–200.

Paldor, N. (1983), Linear stability and stable modes of geostrophic fronts, *Geophys. Astro. Fluid*, *24*, 299–326.

Pedlosky, J. (1982), *Geophysical fluid dynamics*, New York and Berlin, Springer-Verlag.

Perret, G., T. Dubos, and A. Stegner (2011), How large-scale and cyclogeostrophic barotropic instabilities favor the formation of anticyclonic vortices in the ocean, *J. Phys. Oceanogr.*, *41*, 303–328.

Phillips, N. A. (1954), Energy transformations and meridional circulations associated with simple baroclinic waves in a two-level, quasi-geostrophic model, *Tellus*, *6*, 273–286.

Plougonven, R., D. J. Muraki, and C. Snyder (2005), A baroclinic instability that couples balanced motions and gravity waves, *J. Atmos. Sci.*, *62*, 1545–1559.

Poulin, F. J., and G. R. Flierl (2003), The nonlinear evolution of barotropically unstable jets, *J. Phys. Oceanogr.*, *33*, 2173–2192.

Rayleigh, L. (1880), On the stability, or instability, of certain fluid motions, *Proc. London Math. Soc.*, *11*, 57–70.

Ribstein, B., J. Gula, and V. Zeitlin (2010), (A)geostrophic adjustment of dipolar perturbations, formation of coherent structures and their properties, as follows from high-resolution numerical simulations with rotating shallow water model, *Phys. Fluids*, *22*, 116,603.

Ripa, P. (1983), General stability conditions for zonal flows in a one-layer model on the beta-plane or the sphere, *J. Fluid Mech.*, *126*, 463–489.

Ripa, P. (1991), General stability conditions for a multi-layer model, *J. Fluid Mech.*, *222*, 119–137.

Sakai, S. (1989), Rossby-Kelvin instability: a new type of ageostrophic instability caused by a resonance between Rossby waves and gravity waves, *J. Fluid Mech.*, *202*, 149–176.

Satomura, T. (1980), An investigation of shear instability in a shallow water, *J. Meteorol. Soc. Jpn.*, *59*, 148.

Snyder, C. (1995), Stability of steady fronts with uniform potential vorticity, *J. Atmos. Sci.*, *52*, 724–736.

Stone, P. H. (1966), On non-geostrophic baroclinic stability, *J. Atmos. Sci.*, *23*, 390–400.

Sutyrin, G. G. (2007), Ageostrophic instabilities in a horizontally uniform baroclinic flow along a slope, *J. Fluid Mech.*, *588*, 463–473.

Sutyrin, G. G. (2008), Lack of balance in continuously stratified rotating flows, *J. Fluid Mech.*, *615*, 93.

Vanneste, J., and I. Yavneh (2007), Unbalanced instabilities of rapidly rotating stratified shear flows, *J. Fluid Mech.*, *584*, 373.

Yamanaka, M. D. (1985), Inertial oscillation and symmetric motion induced in an inertio-gravity wave critical layer, *J. Meteor. Soc. Japan*, *63*, 715–737.

Yamazaki, Y. H., and W. R. Peltier (2001a), The existence of subsynoptic-scale baroclinic instability and the nonlinear evolution of shallow disturbances, *J. Atmos. Sci.*, *58*, 657–683.

Yamazaki, Y. H., and W. R. Peltier (2001b), Baroclinic instability in an Euler equations-based column model: the coexistence of a deep synoptic-scale mode and shallow subsynoptic -scale modes, *J. Atmos. Sci.*, *58*, 780–792.

Yavneh, I., J. C. McWilliams, and M. Jeroen Molemaker (2001), Non-axisymmetric instability of centrifugally stable stratified Taylor-Couette flow, *J. Fluid Mech.*, *448*, 1–21.